Delft University of Technology

Section of Environmental Fluid Mechanics

Hydraulic Engineering

Setting up a numerical flume using a hybrid particle - mesh method

Author:
Chit Yan Toe
4580389

Supervisors:
Dr. ir. R. J. Labeur
Dr. ir. J. D. Bricker
Ir. J. M. Maljaars

May 13, 2017

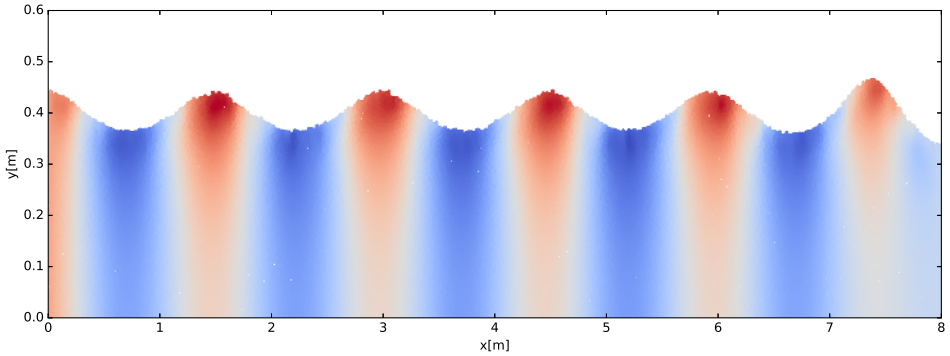

TU Delft

Contents

List of Figures

List of Tables

Abstract

A literature survey which concerns a variety of wave generation and absorption methods was accomplished. The survey deals with the methods used for the experiment wave tank and numerical wave tank. Their implementations are also described very briefly.

The numerical wave tank (NWT) was set up using the hybrid particle-mesh method with the emphasis on the wave generation of solitary wave and linear progressive wave, and passive absorption at the far side of the wave tank. The Discontinuous Galerkin method was applied to solve the Navier-Stokes equations on the background mesh while the particles are used for solving the non-linear advection term. The waves are generated by using a piston-type wavemaker with the use of first-order linear wavemaker theory. For the absorption of reflected waves at the termination end, the sponge layer approach was implemented making use of viscous damping or internal friction among water particles. The hyperbolic tangent function is found to be applicable for smoothly increasing viscosity in the damping zone, which is also be able to prevent the formation of rigid body at the transition point. The drawbacks of the passive absorption technique are not only the extra cost of computational power and domain size, but also the rising slope of average water surface elevation induced by the accumulation of water particles near the end of the wave tank.

The solitary waves of small amplitude could be simulated with reliable accuracy and also did the linear progressive waves in the intermediate water. The short waves and the long waves need to paid more attention for the wave generation boundary condition. Regarding the passive absorption for both of solitary waves and progressive waves, the same hyperbolic tangent function was used for viscosity functions which increases spatially. The solitary wave can be damped out using this function while the latter one cannot be damped, leading to the instability of the computation induced by the loss of the particles in the mesh system.

Chapter 1

Introduction

Different kinds of partial differential equations (PDEs) which can describe the nature of the flow and fluid-structure interaction behaviour, are the main constituents of fluid dynamics. There is still lack of knowledge to solve the non-linear PDEs analytically or in closed form. Therefore numerical methods have become popular to solve the solutions approximately to these equations since the development of digital computers.

In the area of numerical approximation methods, many researchers have been developing the methods in these two well-known frameworks, namely the Eulerian framework and Lagrangian framework. The three well-known numerical approximation ideas are Finite Difference Methods (FDMs), Finite Volume Methods (FVMs) and Finite Element Methods (FEMs). Both of these methods can be applied in the Eulerian framework and Lagrangian framework.

Nevertheless, since there are some drawbacks from these three mesh-based numerical discretizations, the original idea of particle method with the name of "Particle-in-Cell (PIC)" was developed by Harlow (1962). This led to the development of many different particle methods (or) meshless methods and hybrid particle-mesh methods e.g. Smoothed Particle Hydrodynamics (SPH), Material Point Method (MPM) (Chen et al. 2006). In fact, these particle methods are founded on the Lagrangian point of view (Liu and Liu 2003).

Since in the Eulerian/Lagrangian grid-based systems the mesh generation is required as a prerequisite, the mesh generation is difficult to be handled, especially for the complex geometry, in such a way to obtain the accurate solutions. Moreover, the mesh-based systems face the great challenges for solving the problems which consist of the large deformations, deformable boundaries and free surfaces (Liu and Liu 2003) as the accuracy of the solution depends on the refinement of updated mesh. However the grid-based systems has the simplicity of the implementation of the governing equations.

Although the purely Lagrangian meshfree methods such as Smoothed Particle Hydrodynamics (SPH) is best known for tackling discontinuous problems, it is notorious for the requirement of expensive computational power. However these kind of numerical methods have the ability of storing the whole history of each material and lack of mesh connectivity for the fields (pressure and velocity) i.e the nodes move freely.

This is the time again to utilize specific advantages of mesh-based methods and meshless methods, i.e. Eulerian framework and Lagrangian framework. In other words, the governing equations are solved using the Eulerian background mesh while the Lagrangian particles are used for advection (Maljaars 2016).

1.1 Research Question

The wave simulation in which the generated wave signals are not interfered by the reflected wave signals from the termination and the wavemaker end, has been the essential requirement for wave-related experiments. Several researchers have been endeavouring to obtain such a perfect simulation experimentally (Milgram 1965; Ursell et al. 1960) and numerically (Jacobsen et al. 2012; Troch and De Rouck 1999a) to some extent. This research is also an attempt to attain the wave simulations which can result in the wave profile free of reflection using the hybrid particle-mesh method.

Using the Discontinuous Galerkin method which is a different mathematical approach from the previous work of Maljaars (2016) in terms of finite element spaces, the main question to be attempted in this research is as follows:

> Using the hybrid particle-mesh method, which techniques are best suitable for wave generation and wave absorption in the numerical wave tank, and what is their validity for accuracy?

The main question should be divided into the following sub-questions:

1. Which methods are used for wave generation and absorption of waves (for the case of open boundary) in an experimental wave tank and a numerical wave tank?
2. How can the provable method from the above sub-question be applied in the hybrid particle-mesh method, and how to implement it for simple linear and non-linear waves?
3. Do the simulated results have validity against the benchmark tests?

1.2 Research Methods

Research methods can be divided into the following steps:

1. *Understanding the wave generation mechanisms*: To acquire first the knowledge of the wave generation in experimental wave flumes, a literature review is conducted, followed by an investigation of wavemaking boundary conditions in a numerical wave tank. Although the mathematical formulation needs to be shaped for the sake of least reflection from both ends of the tank based on the literature survey, in the current research the re-reflection effect is ignored but only the reflection from the far end is considered to be wiped out in the tank.
2. *Implementing the boundary conditions in the hybrid particle-mesh method*: It will be identified whether the result from the step 1 should be implemented at the particle level or background mesh level. For modifications or imposing these at the mesh level, the FEniCS package will be in use. If it deals with the particle level, more work needs to be done regarding the mapping or projection methods, and/or particle administration (Maljaars 2016).
3. *Validation of simulation results with benchmark cases:* To check the accuracy and reliability of the formulated method, some test cases should be done for comparison against the benchmark cases.

1.3 Research Procedure

The flowchart 1.1 describes the overview of the research process.

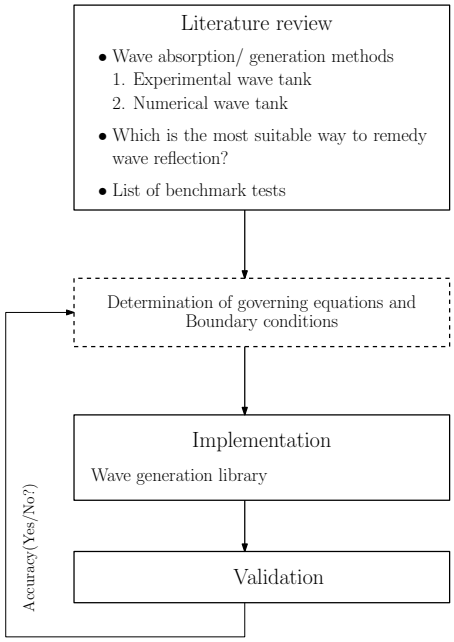

Figure 1.1: Procedure of the research.

1.4 Research Outcomes

The final product of this additional research should be a technical report which describes the implementation of boundary conditions for wave generation and wave absorption in the hybrid particle-mesh method. It will also include the literature review on the generation and absorption methods for numerical wave tank and experimental wave tank. Given the literature review and decision of suitable boundary condition, a library for wave-making boundaries will be devised.

Chapter 2

Literature Review

The simulation of regular waves and irregular waves plays a vital role in the study of coastal engineering, maritime engineering and civil engineering. It becomes necessary to attain targeted wave profiles by means of generation and reflection (or without reflection for the case of progressive waves) in the experimental wave tank (EWT) and numerical wave tank (NWT). The wave generation methods and absorption methods proposed by the researchers for experimental study and numerical simulation are studied in the coming subsections.

The wave generation methods and the wave absorption methods will be reviewed according to the four aspects which are generation at the wavemaker, active absorption, passive absorption at the termination, and combined generation/ absorption mode at the wavemaker.

2.1 Experimental Wave Tank (EWT)

In the laboratory wave flume waves are initiated by moving the plates horizontally, vertically or with inclination driven by the mechanical system at the one end. The motion of the wavemaker determines theoretically the properties of the desired wave types such as the surface elevation, the velocity of the water particle. The trajectory of the wavemaker, which assigns the motion of the plate, needs to be determined based on the wave theories for the required wave shapes.

The simulated wave profiles are dependent on the wavemaker properties such as the position of the wavemaker, its shape (circular, plate, curved plate) and its orientation. Detailed information about a variety of wavemaker positions and shapes is provided in the report "Laboratory wave-generating apparatus" (Pilch 1953). The common type for generating shallow-water waves is the piston-type wavemaker because the motion of wavemaker plate more is closely similar to the water particle trajectories under the waves, whereas the one for deep-water wave simulation is the paddle-type wavemaker hinged at some level above or at the bottom of the flume (Dean and Dalrymple 1991).

2.1.1 Generation of regular and irregular waves

Havelock (1929) formulated generically the linear wavemaker theory using the velocity potential of linear wave theory, which means that the theory is valid only for small amplitude of harmonic motion and irrotational flow. Galvin (1964) was one who reasoned the volume of water in the wave crest must be the same as the water volume displaced by the motion of wavemaker (Dean and Dalrymple 1991). The relationship between the wavemaker motion and the surface elevation of the wave is derived based on this reasoning and Havelock's linear wavemaker theory (Dean and Dalrymple 1991).

Ursell et al. (1960) attempted the wavemaker theory for piston-type wavemaker in an experimental wave flume, and found out the small-amplitude wave theory could work well for small wave steepness ($0.002 \leq H/L \leq 0.03$). Multer and Galvin (1967) have observed that the waves generated by linear wave maker theory lost their shape while propagating, then breaking down several components into primary wave and secondary components (as cited by Madsen (1971)). Madsen (1971) introduced a motion which is able to suppress undesirable harmonics in order to get the permanent waveform, using the "second-order wavemaker theory".

The second-order wavemaker theory was extended for generating irregular waves by Schäffer (1996). A

second order wavemaker theory which can reduce the computing time of the controller for the generation of regular waves and irregular waves was introduced by Petit et al. (1993) even though they found some discrepancies between the experiment and the theoretical results due to limited analysis. However, in the present research the second-order wavemaker theory was not included.

For generation of long waves including the solitary wave and cnoidal wave, Goring (1978) derived the stroke trajectory of piston-type wavemaker using the Boussinesq-type solitary wave solution. In his experiment it was observed that it took a duration to separate the solitary wave from the trailing waves since the initially generated solitary wave was contaminated by some oscillatory waves. Malek-Mohammadi and Testik (2010) developed a new methodology for Boussinesq-type and Rayleigh-type solitary wave generation slightly different from Goring's methodology by taking into account the evolving process of the solitary wave during the generation phase. This new methodology ensures that the generated wave gains the permanent wave form within a shorter duration and less dissipative compared to the methodology of Goring (1978).

Katell and Eric (2002) studied the solitary wave generation using four different kinds of wave solutions i.e. Boussinesq-type (applied by Goring (1978)), shallow water first order/KdV, shallow water second order, and Rayleigh-type. The paddle motion induced by Rayleigh-type solution could give rise to purer solitary waveform than the waveform derived from the rest solutions, and attain the solitary wave more faster. The trailing waves also occur in the initial stage but smaller than the ones in Goring's experiment (Goring 1978).

Zhang and Schäffer (2007) presented the new technique for highly non-linear wave generation using the Stream function theory which lacks the restriction of irrotational flow, so-called "approximate Stream function wavemaker theory". It was composed of two steps, namely time-integration of depth-averaged velocity in a Lagrangian perspective following the wave paddle position as done by Goring (1978), and correction for dispersion effect to paddle motion . This wavemaker theory is only valid in shallow and intermediate waters but it fails to generate correctly in deep water because the dispersion correction in the second step is done based on linear wavemaker theory (Zhang and Schäffer 2007).

As the latest one of this research trend, Aknin and Spinneken (2017) did extensive study on wave generation by using position-control system and force-control system (detailed by Spinneken et al. (2009)) for the purpose of investigating the dependency of water depth on the latter one. They presented the correction terms for force-control generation in the case of piston-type wavemaker, noticing the contamination of free wave during generation. By doing so they successfully eliminated the super harmonic free wave in the shallow and intermediate waters using Stream function in force-control generation. Andersen et al. (2016) also claimed that using high quality wavemaker theory (e.g. approximate Stream function) could give rise to the most exact form of regular waves.

2.1.2 Absorption of reflected and re-reflected waves

The question how to prevent reflection from the termination and re-reflection from the generator arose from the requirement of getting the reflection-free wave profile. Herbich (1956) extensively investigated on the wave absorption by using the absorbers at the termination of the flume and filters at the generator, so-called the passive absorption. In the passive absorption method, the incident waves arriving at the termination and generator are damped via energy dissipation using specific materials (e.g. cellular wire mesh, sloping beach, perforated plates). The reflection coefficient is dependent on the proposed absorptive materials and its properties as well as wave characteristics.

Milgram (1970) attempted to remove the wave reflection from the far end by using the active absorption, which cannot be eliminated by Ursell et al. (1960) who validated the linear wavemaker theory. The active absorption technique includes that the right boundary of the wave tank moves systematically in such a way the incoming waves seem to pass through it. Salter (1981) applied active absorption at the wavemaker, so-called "combined generation/absorption mode" for the paddle. This attempt is a means to mitigate the re-reflection of the incident waves at the wavemaker. If the absorption method is applied at both sides of the tank, the termination end and/or the wavemaker end is movable in such a way to cancel out the incident waves facing it by producing a wave motion. This wave motion is obtained via the digital or analogue filter using the information of the corresponding incident waves such as surface elevation and velocity.

Since the design of filter system is crucial part in the active absorption method, many researchers

have studied how to modify the response function of the filter in order to absorb correctly and save the delay time. Andersen et al. (2016) recently proposed to use FIR (Finite Impulse Response) filter instead of IIR (Infinite Impulse Response) filter which can accumulate the error if there is a small error, for example, in water level during testing. It has been shown that the proposed method worked for both of regular and irregular waves generation in which they turned on absorption mode at both sides.

Regarding the position of detecting wave information before the wave paddle, Hald et al. (1997) presented the theoretical frequency response of filter systems for three kinds of active absorption: measuring the surface elevations ($\eta - \eta$) system, measuring the surface elevation and the velocity ($\eta - u$) system, and measuring the velocities ($u - w$) system. That means two measurements of elevation and velocity are done before the waves arrive back the wave plate because they tested for combined absorption/generation mode while the fully reflective walls are installed at the end of the tank. The former two systems are carried out in their experiments proving good quality of absorption even at highly reflective conditions.

2.1.3 Conclusion

The higher-order wavemaker theory has been proven to generate the most accurate wave forms although the computation time for controller in the wavemaker is a considerable factor. Moreover the underlying wave theory used for constructing the wavemaker motion also determines the accuracy of required waveform. For instance, in order to generate solitary wave, different wave solutions (e.g Rayleigh solution, Boussinesq solution) are available to be used for wavemaking with their own advantages and disadvantages i.e. contamination of trailing waves, wave profile development and stability.

The active absorption method for wave reflection is more cumbersome to be implemented than the passive absorption since the former one requires the analogue/ digital filters to control wave plate motion, which in turns generate the compensating waves. Indeed the reflection coefficient is dependent on the wave characteristics of the incident waves as well as the properties of absorbers and filters in case of passive absorption.

2.2 Numerical Wave Tank (NWT)

The wave generation in the numerical wave tank can be done based on the wavemaker theories applied in experimental wave flumes. Although the underlying concepts for wave generation and absorption behind these two kinds of wave tanks are the same, their actual mechanism are slightly different in terms of implementation on mathematical ground and physical ground respectively. It means that in the EWT the waves cannot be created without any movement of the plate or material whereas in the NWT it is possible to produce the waves without any movement of the boundary plate, but by mathematically prescribed function. Moreover the plate movement in the NWT can be performed as explained by the section 2.2.3.

Since the boundary conditions are the main components of any numerical modelling problems as they can lead to non-realistic solutions, many researchers have been endeavouring to determine which boundary condition is the most suitable for wave generation and wave absorption. They are still challenging tasks for exact wave simulations in NWT. The following subsections are devoted to the mathematical techniques for wave generation, or description of boundary conditions, which are mainly responsible for the motion of water particles.

The common methods for wave generation and absorption are listed below and briefly explained later:

1. Wave generation
   (a) Boundary generation approach
   (b) Internal source approach
   (c) Wave paddle approach
2. Passive absorption

2.2.1 Boundary generation approach

Higuera et al. (2013) set up an NWT which is capable of reliable wave generation with active absorption system at the termination, using the VOF type model (a method of free-surface tracking), namely the OpenFOAM® solver. They applied “boundary generation” approach for wave generation, in which the

motion of the water surface at the boundary position is described by the analytical solution for wavemaker theory of which the function can be in velocity or free surface at the paddle. In the boundary generation approach, one has to specify the velocity components and surface elevation at the initial position x_0 by using any wave theory (Troch and De Rouck 1999a). In this approach, the boundary will not move in space, but fixed at horizontal dimension.

As the governing equations in this approach, the momentum equations and continuity equation were used for 2-dimensional $x-z$ plane by Troch and De Rouck (1999a) as given below respectively:

$$\frac{\partial \vec{u}}{\partial t} + (\vec{u}\cdot\nabla)\vec{u} + \frac{1}{\rho}\nabla p = \nu\left(\nabla^2\vec{u}\right) + \vec{g} \tag{2.1}$$

and

$$\nabla\cdot\vec{u} = 0 \tag{2.2}$$

where $\vec{u}$ is the velocity vector, ν is the kinematic viscosity, and $\vec{g}$ is the gravity vector. The definition of boundary condition at the left side of the wave tank could be done by assigning the velocity vector, $\vec{u}(x_0,z,t)$ and the surface elevation, $\eta(x_0,t)$ with the use of linear wave theory.

Similarly Troch and De Rouck (1999a) used VOF type model to test active wave generating-absorbing wavemaker while they applied a sponge layer which is highly viscous material (which is explained later) at one end to absorb waves. They recommended to use velocity information for filter design rather than surface elevation in the case of active absorption since the latter one is computationally time consuming. Spinneken et al. (2014) presented state-of-the-art active absorption-generation wavemaker using force-feedback technique which can automatically respond to incident waves considering the ideal fluid.

In short, the generation method just mentioned above is the combination of boundary generation approach and active absorption technique, which is quite complicated for designing the filter function (analogous to EWT section 2.1.2). Since this research does not cover this type of wave generation and absorption, it will be omitted here. Actually it would have been attractive numerically for its simplicity of implementation to use this type of wave generation, although it is not realistic from the experimental point of view.

2.2.2 Internal source approach

The internal source approach was devised as a substitute of active wave generating-absorbing boundary condition about which is explained in section 2.2.3. Due to some undesirable effects in this method (2.2.3), such as error accumulation in longer simulation, Lin and Liu (1999) innovated a new method, so-called "internal source approach" in which active absorption boundary is not required any more, since only a radiation boundary condition is needed. The waves are generated by internal mechanism inside the computational domain, in which a mass source function which is added to the continuity equation or the momentum equation.

The source function needs to be designed in such a way not to interact with waves reflected from the ends, and in principle provided a source function, any kind of wave can be generated (Lin and Liu 1999). For instance, if a particular mass source function $s(x,y,t)$ is added to the continuity equation, the following obtains:

$$\frac{\partial u}{\partial x} + \frac{\partial v}{\partial y} = s(x,y,t) \qquad \text{in} \qquad \Omega \tag{2.3}$$

Again the source function can be derived using the expected time history of free surface displacement $\eta(t)$ above the source region as follows:

$$\int_0^t \int_\Omega s(x,y,t)\, d\Omega\, dt = 2\int_0^t C\ \eta(t)\, dt \tag{2.4}$$

with the assumption that the the contribution of source function is completely effected on the generated wave. The factor 2 in the equation 2.4 indicates the source region is located in the middle of wave tank, and C denotes the phase velocity of the required wave. Such a method worked well in accordance with the theories for linear regular and irregular waves, Stokes wave, cnoidal wave and solitary wave.

2.2.3 Wave paddle approach

The wave paddle approach is derived from the concept of constructing solid body in the NWT similar to moving wave plate in EWT (Chen et al. 2016). It means that the wave paddle in EWT is mimicked by one

in the NWT by means of (numerical) particles or mesh. The main question arising in this approach is how to construct a solid body in terms of mathematical formulation as much exact as possible, and how to determine the fluid-structure interaction.

Oliveira et al. (2012) applied the Particle Finite Element Method (PFEM) for conceptualizing the wave paddle in NWT of which the motion is described by the wavemaker theory. The concept of fluid-structure interaction was used by them to construct the wave paddle by means of numerical solid body. This numerical solid body (wave paddle) will move to generate the waves according to the displacement function of the wavemaker theory. The simulated results of the test cases captured well the experimental results.

The construction of this numerical method will be discussed shortly. The PFEM is distinct from classical Finite Element Method (FEM) in terms of remeshing technique and evaluation of boundary position at single time step (Oliveira et al. 2012). In fact, the PFEM is a type of hybrid particle-mesh method in which the mesh is constructed at each time step and particles are used for elimination of mesh connectivity and non-linear convection term in the momentum equations (Idelsohn et al. 2004).

In the PFEM formulation, the governing equations are discretized on the particles instead of on the traditional mesh, using the interpolation functions. Since there is no definition of boundary surface or line in the particle configuration, the mesh became necessary to evaluate the acting forces on the domain. That is why they chose the method of evaluating the forces by solving a continuous differential equation in the entire domain, instead of finding the interacting forces between the particles with the use of local contact problem.

Therefore in order to find out the external forces on each particle via imposing the boundary condition on a defined boundary surface, the mesh is created at each time step to solve the Navier-Stokes equations. After evaluating the forces, the old mesh will disappear and then the new mesh will be created again for at the new time step depending on the solution of the previous time step (Idelsohn et al. 2004).

Similarly Chen et al. (2016) applied Particle-in-cell solver for incompressible free surface flows (PICIN) for paddle movement in the NWT. The PICIN was originally developed by Kelly et al. (2015) for two-way coupling of fluid-solid interaction. Chen et al. (2016) defined the wavemaker using the cut-cell approach which is a method of grid generation detailed by Ingram et al. (2003), and a relaxation zone for wave absorption. The PICIN demonstrated satisfactorily the non-linear processes of wave generation using a relaxation method.

In the framework of particle methods, the new approach for wave absorption is presented as active absorption where it was applied at the termination, by Shibata et al. (2011) using Moving Particle semi-implicit Method (MPS). Similar to the active absorption method, after the information of the incident wave is obtained, the water particles on the boundary are enforced to move accordingly in order to absorb the waves. In this transparent boundary approach, the particles are administered with the help of the particle generation and deletion algorithm to prevent the particle requirement and overfull particle respectively.

Moreover, the ratio of wave height to the paddle stroke is an essential requirement for the wave paddle approach because the desired wave profile such as wave amplitude and wave height can be produced only by the accurate movement of the wave plate. The following derivation of the wave height to stroke ratio is extracted from the book of Dean and Dalrymple (1991). The whole story is laid down on the Laplace equation or potential flow theory in $x-z$ plane:

$$\frac{\partial^2\phi}{\partial x^2}+\frac{\partial^2\phi}{\partial z^2}=0 \tag{2.5}$$

with the linearized form of the dynamic and kinematic free surface boundary conditions at $z=0$:

$$\eta=\frac{1}{g}\frac{\partial\phi}{\partial t} \tag{2.6}$$

$$-\frac{\partial\phi}{\partial z}=\frac{\partial\eta}{\partial t} \tag{2.7}$$

and bottom boundary condition (no-flow condition) at $z=-h$:

$$-\frac{\partial\phi}{\partial z}=0 \tag{2.8}$$

If $S(z)$ is the the stroke of the wavemaker, the function for its horizontal displacement should be as follows:

$$x = \frac{S(z)}{2}\sin(\sigma t) \tag{2.9}$$

where σ is the wavemaker frequency. Therefore the functional form for an expression of the wavemaker movement would be given below:

$$F(x,z,t) = x - \frac{S(z)}{2}\sin(\sigma t) = 0 \tag{2.10}$$

Using the equations just mentioned above, the lateral boundary condition for the wave tank can be derived and it should be used for solving the Laplace equation 2.5. This lateral boundary condition is given by:

$$u(0,z,t) = \frac{S(z)}{2}\sigma\cos(\sigma t) \tag{2.11}$$

In fact, there exists an infinite number of solutions to the equation 2.5 which can be expressed generally:

$$\phi = A_p\cosh\{k_p(h+z)\}\sin(k_p x - \sigma t) + \sum_{n=1}^{\infty} C_n e^{-k_s(n)x}\cos\{k_s(n)(h+z)\}\cos(\sigma t) \tag{2.12}$$

where the subscripts $[]_p$ and $[]_s$ denote for the progressive wave and standing waves respectively. The unknown constants A_p and C_n need to be determined for the specific solution and hence the boundary condition 2.11 is used to obtain it.

After a lengthy mathematical manipulation, the value of A_p is determined as below:

$$A_p = -\frac{2S\sigma\sinh\{k_p h\}}{k_p\left[2k_p h + \sinh\{2k_p h\}\right]} \tag{2.13}$$

in which S is the expression of $S(z)$ for the piston motion since the stroke is constant over the depth. For the flap motion or hinged paddle motion, the expression of $S(z)$ would be $S(z) = S(1+\frac{z}{h})$. It also should be noted that there exists two equations for the wave height of the progressive wave as below:

$$\eta = -\frac{A_p}{g}\sigma\cosh\{k_p h\}\cos\{k_p x - \sigma t\} \tag{2.14}$$

$$\eta = \frac{H}{2}\cos\{k_p x - \sigma t\} \tag{2.15}$$

These two equations lead to the following equation:

$$\frac{H}{2} = -\frac{A_p}{g}\sigma\cosh\{k_p h\} \tag{2.16}$$

Finally inserting the equation 2.13 of A_p into the equation 2.16 gives the wave height to paddle stroke ratio:

$$\frac{H}{S} = \frac{2\left[\cosh\{2k_p h - 1\}\right]}{2k_p h + \sinh\{2k_p h\}} \tag{2.17}$$

for the piston type motion or for generation of long waves in shallow water where the horizontal components of the particle velocity are almost constant over the water depth. For the deep water waves, the hinged paddle should be used and its ratio of the wave height to the stroke is also given by:

$$\frac{H}{S} = 4\frac{\sinh\{k_p h\}}{hk_p}\frac{\left[hk_p\sinh\{k_p h\} - \cosh\{k_p h\} + 1\right]}{2k_p h + \sinh\{2k_p h\}} \tag{2.18}$$

2.2.4 Passive absorption

Regarding the passive absorption method, two kinds of implementations are available for any technique of wave generation. These two implementations of wave absorption are (1) adding artificial viscosity in the governing equations or sponge layer approach (Cao et al. 1993), and (2) adding the damping term in the free surface boundary conditions near the right side of the tank or in the damping zone (Celebl et al. 1998).

For the first approach of wave absorption, a linear artificial damping term $\nu\vec{u}$ was added in the momentum equation by Chan (1975) (as cited by Cao et al. (1993)) as follows:

$$\frac{\partial\vec{u}}{\partial t} + (\vec{u}.\nabla)\vec{u} + \nabla p + \vec{k} + \nu(x)\vec{u} = 0 \tag{2.19}$$

where ν is 0 outside the damping zone. The artificial damping parameter $\nu(x)$ was formulated such that $\nu = \nu_0 \left(\frac{x-x_l}{L-x_l}\right)^2$ inside the absorbing beach and $\nu = 0$ for the rest. The formulation of the artificial damping term should be different for different wave simulations depending on the wave properties.

The research conducted by Israeli and Orszag (1981) is remarkable for deep investigation on the artificial damping which consists of the viscous damping and internal friction damping. They introduced the system of equations imposing the damping based on the original equation $\frac{\partial^2 u}{\partial t^2} = \frac{\partial^2 u}{\partial x^2}$, which is given by:

$$\begin{aligned} \frac{\partial v}{\partial t} &= \frac{\partial w}{\partial x} + \mu(x)\frac{\partial^2 v}{\partial x^2} - \nu(x)v \\ \frac{\partial w}{\partial t} &= \frac{\partial v}{\partial x} \end{aligned} \tag{2.20}$$

where $v = \frac{\partial u}{\partial t}$ and $w = \frac{\partial u}{\partial x}$. In that case, $\mu(x)$ denotes a linear viscous damping coefficient while $\nu(x)$ is a linear "Newtonian cooling" or "friction" coefficient which is similar to that of Cao et al. (1993). They observed that the usage of $\nu(x)$ outweighs that of $\mu(x)$ by the rate of damping energy. Moreover the damping provided by the $\nu(x)$ can absorb the wide range of wavelengths.

Explained more about the above statement by Cao et al. (1993) using the mathematical descriptions, it should start with the steady wave solutions of equation 2.20:

$$v(x) = e^{ikt - iax} \tag{2.21}$$

where

$$\alpha = k\left(\frac{1 - iv/k}{1 + i\mu k}\right)^{\frac{1}{2}}$$

with $\nu(x) \equiv \nu$ and $\mu(x) \equiv \mu$. While the damping rate is $-\mathrm{Im}\,\alpha$, for $\nu = 0$:

$$\begin{aligned} -\mathrm{Im}\,\alpha &\sim \tfrac{1}{2}\mu k^2 \qquad (k \to 0), \\ -\mathrm{Im}\,\alpha &\sim \left(\tfrac{k}{2\mu}\right)^{0.5} \qquad (k \to \infty) \end{aligned} \tag{2.22}$$

and for $\mu = 0$:

$$\begin{aligned} -\mathrm{Im}\,\alpha &\sim \left(\tfrac{1}{2}\nu k\right)^{0.5} \qquad (k \to 0), \\ -\mathrm{Im}\,\alpha &\sim \left(\tfrac{1}{2}\nu\right) \qquad (k \to \infty) \end{aligned} \tag{2.23}$$

Given the constant μ or ν, if the Newtonian cooling method is used, the damping rate $-\mathrm{Im}\,\alpha$ does show more variation as a function of k. Besides, as $\nu \to \infty$ with $\mu = 0$ for constant k, $-\mathrm{Im}\,\alpha \to \infty$, leading to huge damping of waves. However with $\nu = 0$ as $\mu \to \infty$, $-\mathrm{Im}\,\alpha \to 0$ for a fixed k, especially short waves, so only a little amount of damping can be achieved. Eventually it could be concluded that the Newtonian cooling coefficient $\nu(x)$ could damp out the wide range of wavelengths with high rate of damping rather than the viscous damping coefficient $\mu(x)$ does. Anyway, the drawback of the artificial damping methods is the requirement of an extra computational space for accommodation of wave energy damping in the NWT.

Despite observing the advantage of the Newtonian cooling parameter over that of viscous damping parameter in this literature, it should be noted that it was investigated using the wave equation. Due to the lack of previous researches doing this study for the Navier-Stokes equations model, the $\nu(x)$ term is omitted in the current research as well.

Kim et al. (2014) also studied the effectiveness of second type of passive absorption in the 3-dimensional NWT using the Laplace equation. The damping terms appear in the kinematic and dynamic free surface boundary conditions specified for damping zone unlike the ordinary free surface conditions. The difference between this case and the aforementioned one is the mechanism of energy losing in the sponge layer i.e. the damping terms inside the momentum equations provide internal friction within the fluid domain while in this method the modified free surface boundary conditions will extract energy from the waves via the additional term P (Cao et al. 1993):

$$\frac{\partial \phi}{\partial t} + \frac{1}{2}\nabla\phi \cdot \nabla\phi + p + z + P = 0 \tag{2.24}$$

where P vanishes outside the absorbing zone, considered as the additional pressure acting on the free surface. In his paper, the term $P = \nu v$ was cited from other researches to demonstrate the working mechanism. This is more applicable to the potential or ideal fluid having no viscosity and no internal

friction.

Therefore using the Laplace model, Kim et al. (2014) analysed five kinds of artificial damping methods using various ramp functions which can avoid the abrupt transition. These five damping methods are displayed in the table 2.1.

Method	Type	Free surface boundary conditions in the damping zone
Method 1	ϕ_n type	D.F.S.C.: $\frac{\mathrm{D}\phi}{\mathrm{D}t} = -g\eta - \frac{1}{2}\lvert\nabla\phi\rvert^2 + \frac{\mathrm{D}\eta}{\mathrm{D}t}\frac{\partial\phi}{\partial z} - \mu_1\frac{\partial\phi}{\partial n}$
		K.F.S.C.: $\frac{\mathrm{D}\eta}{\mathrm{D}t} = -\nabla\phi\nabla\eta + \frac{\partial\phi}{\partial z}$
Method 2	ϕ type	D.F.S.C.: $\frac{\mathrm{D}\phi}{\mathrm{D}t} = -g\eta - \frac{1}{2}\lvert\nabla\phi\rvert^2 + \frac{\mathrm{D}\eta}{\mathrm{D}t}\frac{\partial\phi}{\partial z} - \mu_1\phi$
		K.F.S.C.: $\frac{\mathrm{D}\eta}{\mathrm{D}t} = -\nabla\phi\nabla\eta + \frac{\partial\phi}{\partial z}$
Method 3	$\phi - \phi_n$ type	D.F.S.C.: $\frac{\mathrm{D}\phi}{\mathrm{D}t} = -g\eta - \frac{1}{2}\lvert\nabla\phi\rvert^2 + \frac{\mathrm{D}\eta}{\mathrm{D}t}\frac{\partial\phi}{\partial z} - \mu_1\phi - \mu_2\frac{\partial\phi}{\partial n}$
		K.F.S.C.: $\frac{\mathrm{D}\eta}{\mathrm{D}t} = -\nabla\phi\nabla\eta + \frac{\partial\phi}{\partial z}$
Method 4	$\eta - \phi$ type	D.F.S.C.: $\frac{\mathrm{D}\phi}{\mathrm{D}t} = -g\eta - \frac{1}{2}\lvert\nabla\phi\rvert^2 + \frac{\mathrm{D}\eta}{\mathrm{D}t}\frac{\partial\phi}{\partial z}$
		K.F.C.S.: $\frac{\mathrm{D}\eta}{\mathrm{D}t} = -\nabla\phi\nabla\eta + \frac{\partial\phi}{\partial z} - \mu_1\eta - \mu_2\phi$
Method 5	$\phi_n - \eta$ type	D.F.S.C.: $\frac{\mathrm{D}\phi}{\mathrm{D}t} = -g\eta - \frac{1}{2}\lvert\nabla\phi\rvert^2 + \frac{\mathrm{D}\eta}{\mathrm{D}t}\frac{\partial\phi}{\partial z} - \mu_1\frac{\partial\phi}{\partial n}$
		K.F.S.C.: $\frac{\mathrm{D}\eta}{\mathrm{D}t} = -\nabla\phi\nabla\eta + \frac{\partial\phi}{\partial z} - \mu_2\eta$

Table 2.1: Five artificial wave damping method (Kim et al. 2014)

The D.F.C.S and K.F.C.S stand for dynamic and kinematic free surface boundary conditions respectively. It was found that the damping method consisting of two damping terms, contrary to other methods of only one damping term, showed the better damping performance.

For instance, one of the artificial damping methods which consist of two damping terms, so-called "$\phi_n - \eta$" type, can be expressed again in the Mixed Eulerian-Lagrangian framework as below:

$$\frac{D\phi}{Dt} = -g\eta - \frac{1}{2}|\nabla\phi|^2 + \frac{D\eta}{Dt}\frac{\partial\phi}{\partial z} - \mu_1\frac{\partial\phi}{\partial n} \tag{2.25}$$

for D.F.S.C using the velocity potential ϕ, and for K.F.S.C the following function is applied in the damping zone:

$$\frac{D\eta}{Dt} = -\nabla\phi\nabla\eta + \frac{\partial\phi}{\partial z} - \mu_2\eta \tag{2.26}$$

where μ_1 and μ_2 are the damping coefficients. The ramp function $\mu(x)$ is used for avoiding the abrupt change in wave quantity, in other words, to make sure that the damping coefficient changes smoothly along the damping zone. The four kinds of ramp functions are presented in that paper, and for example one of these is as below:

$$\mu(x) = \mu_0 \sin\left\{\frac{\pi}{2}\left(\frac{x - x_d}{l_d}\right)\right\} \tag{2.27}$$

where l_d is the total length of damping zone, $x - x_d$ is the local length of damping zone, and μ_0 is the targeted damping coefficient.

Likewise, the relaxation method used by Chen et al. (2016) is indeed similar to the concept of the artificial damping methods mentioned earlier. In this method the absorption function $a(x)$ is applied on the computed velocity and surface elevation in the area of sponge layer after every computation time step. It means that after each time step the computed quantity is enforced to the relaxation quantity given by

$$\phi = a(x)\phi_{\text{computed}} + (1 - a(x))\phi_{\text{target}} \tag{2.28}$$

where ϕ is surface elevation or velocity. The ϕ_{target} can be obtained using the analytical value (Jacobsen et al. 2012). The absorption function, for instance, is in a following form:

$$a(x) = \sqrt{1 - \left(\frac{x - x_1}{x_s}\right)^2} \tag{2.29}$$

where x_1 is the starting point of the sponge layer while x_s is the sponge layer length (Troch and De Rouck 1999b). The function starts from 1 at the start of the layer and ends at 0. The detailed numerical implementation of the novel sponge layer approach is referred to the research of Larsen and Dancy (1983).

2.2.5 Conclusion

Of the available wave generation techniques, the wave paddle approach is quite similar to the actual wavemaker of EWT if the fluid-structure interaction can be simulated well. In the wave paddle approach of the NWT, the way of wave absorption needs to be determined whether relaxation methods or active absorption should be used. However the internal source function method can be used for the NWT without any consideration of absorption methods, but in the hybrid particle-mesh methods, it needs to be researched for nonlinear waves generation.

The boundary generation approach has been proved feasible in the Eulerian framework (VOF type model) with a combination of passive absorption or active absorption. Moreover it can be also applied in case of Lagrangian methods. In fact, different combinations of generation methods and absorption methods is possible.

In this research, the wave paddle approach seems suited to be applied in the hybrid particle-mesh method since it does not require long computational zone like in the internal source approach. Moreover it does not need analytical solution of wave profile which should be applied at the boundary. However, there is one problem in particle distribution when the boundary plate of the NWT moves, leading to the empty cells near the boundary. To circumvent this problem the moving mesh is introduced so that the mesh boundary is aligned with the prescribed boundary velocity (Maljaars 2016). Therefore the method requires the function of the paddle motion i.e. solution of the wavemaker theory.

Regarding the absorption method for the present research, the passive method appears more suitable than active method though the former one is computationally intensive due to longer computational area. Moreover since the active absorption method requires complicated mathematical functions for filter design, the passive way which does need only wave relaxation functions, seems doable in the context of hybrid particle-mesh numerical method.

Chapter 3

Viscosity effect on the dam break problem

The role of viscosity plays an important role in dissipation of forces or wave energy in both of EWT and NWT. The preliminary study on effect of viscosity on flow motion is done using the dam break problem. In fact the dam break problem is a benchmark test widely used for validations of numerical simulation results in computational hydraulics (Mast 2013; Cherfils et al. 2012). The mechanism of the dam break simulation is that the water column collapses due to the gravity when the gate or barrier holding the water is removed. Immediately after the lack of the gate, the water starts to flow out and impacts to the other side of the boundary, and back and forth.

The objective of this study is to realize how the viscosity affects the flow velocity and motion of the dam break flow, and which kind of viscosity function should describe the highly damped motion of dam break flow. The highly damped motion of the flow means that the front part of the water domain should not propagate in infinite time, or at least it should move with infinitesimal speed and without any chaotic motions unlike turbulent flow.

The knowledge of this section will be employed in the next chapter of numerical wave simulation where the artificial damping method is used. Since the requirement of the wave absorption in this method is to avoid the sudden change of wave property, the smoothly increasing shape of damping function is desirable to use in the NWT. Likewise, in the present section, some mathematical functions will be tested to observe if the motion of the dam break flow will be damped or not in a longer time simulation.

3.1 Governing equations and Boundary conditions

Before proceeding with the governing equations of the problem, the procedure of the hybrid particle-mesh method should be mentioned briefly for clear understanding of solving the differential equations. It should be noted that the underlying governing equations and numerical discretizations also hold the same for the wave generation problem (4), while the different boundary conditions are applied for both cases respectively.

The present hybrid particle-mesh method is composed of the following four steps (Maljaars 2016):

1. *Particle projection to the mesh:* The information owned by the particles are mapped onto the mesh which will serve the background for solving the equations in the next step. A least square projection method, for instance, can be applied to do the task by solving the following equations:

$$\sum_p N_i(\mathbf{x}_p) N_j(\mathbf{x}_p) \rho_j = \sum_p N_i(\mathbf{x}_p) \rho_p \tag{3.1}$$

$$\sum_p N_i(\mathbf{x}_p) N_j(\mathbf{x}_p) \mathbf{u}_j = \sum_p N_i(\mathbf{x}_p) \mathbf{u}_p \tag{3.2}$$

   where ρ_j and $\mathbf{u}_j$ denote the nodal density and velocity unknowns at the background mesh, respectively. The ρ_p and $\mathbf{u}_p$ in the equations above represent the particle density and velocity for the particle p while $N_{i,j}$ are nodal basis functions evaluated at the particle position at $\mathbf{x}_p$.

2. *Solving the equations on the background mesh:* The governing equations are solved using the mesh or grid system by means of FEM, FVM or FDM. The incompressible Navier-Stokes (NS) equations

which consist of conservation of momentum equation and continuity equation, are the governing equations for this research. For the flow domain Ω within the time frame $I = (t^0, t^N)$, the NS equations are expressed as below:

$$\rho \frac{\mathrm{D}\mathbf{u}}{\mathrm{D}t} = \mathbf{f} - \nabla p + \nabla \cdot \boldsymbol{\sigma} \qquad \text{in} \qquad \Omega \times I \tag{3.3}$$

$$\nabla \cdot \mathbf{u} = 0 \qquad \text{in} \qquad \Omega \times I \tag{3.4}$$

where: $\mathbf{u}$ denotes the flow velocity, ρ the density, p the pressure, $\mathbf{f}$ the body force, and σ the viscous stress tensor defined by $\sigma = 2\mu\nabla^s\mathbf{u}$, with $\nabla^s(.) = \frac{1}{2}\nabla(.) + \frac{1}{2}\nabla(.)^T$ being the symmetric gradient operator and μ is the dynamic viscosity. The treatment of the boundary conditions are explained later in the section 4.0.1.

A variety of numerical methods can be used to solve the equations 3.3-3.4 using the background mesh. In this research the FEniCS computing platform which was built upon the FEM method is deployed to do this task. Since the FEniCS is designed to automate the solution of any differential equations under the FEM framework, the user of this computing platform has his own freedom to formulate the governing equations (or strong form) into various kinds of variational equations (or weak form) and to create their corresponding function spaces. This leads to the possibility for using different FEM methods and function spaces for avoiding some numerical artefacts.

In this thesis, the hybrid finite element method which makes use of the Discontinuous Galerkin (DG) method formulated by Labeur and Wells (2012), is applied for solving the equations 3.3-3.4 which has the advantage of stabilizing feature inherited from DG method in case of advection-dominated flows.

3. *Mesh mapping to the particle:* The results (or quantities) resulting from the background mesh in the previous step are transferred to the particles. The interpolation between the mesh and the particle becomes necessary for mapping the newly resulted information. The interpolation techniques in the well-known hybrid particle-mesh methods such as PIC and FLIP are in hand for this mapping task. In the present research, the PIC approach is used for the sake of suppressing the high-frequency fluctuations.

4. *Movement of the particles:* The particles are updated with newly acquired velocity and then advected to new position. The equation 3.5 determines the particle advection for each particle p:

$$\frac{\mathrm{d}\mathbf{x}_p(t)}{\mathrm{d}t} = \tilde{\mathbf{u}}_p(\mathbf{x}_p, t) \tag{3.5}$$

where

$$\tilde{\mathbf{u}}_p(\mathbf{x}_p, t) = \sum_i \tilde{N}_i(\mathbf{x}_p)\tilde{\mathbf{u}}_i(t)$$

in which $\tilde{N}_i$ is the velocity interpolant. To solve the ordinary differential equation 3.5 the Runga-Kutta numerical scheme is used for high accuracy.

3.2 Dam break model

The model of dam break problem developed by (Maljaars 2016) which was constructed using the hybrid particle-mesh method, was used for the study of viscosity. The schematization of the problem is depicted in the figure 3.1a which represents the water particles as the blue dots. The free surface flow occurs due to the gravity once the gate is removed, and then the position of the particles changed dramatically as shown in the figure 3.1b. The initial model setting (table 3.1) was applied to acquire the knowledge of viscosity effect on the flow velocity of the dam break. Using the general setting, the model was simulated with the different values and functions representing the viscosity parameter. It should be noted that the viscosity does not change over the range of the computational domain i.e. $\mu_{\text{water}} = \mu_{\text{air}}$.

3.2.1 Simulation results and Conclusion

3.2.1.1 Constant viscosity

In the first group of simulations (figures 3.2a - 3.3c) in which the constant value of viscosity was used for both water and air. The simulated time is 0.75 s in these simulations while in the case of $\mu = 0.1$ (figure 3.2a) the computation stopped due to numerical instability which is the reason of particle spacing

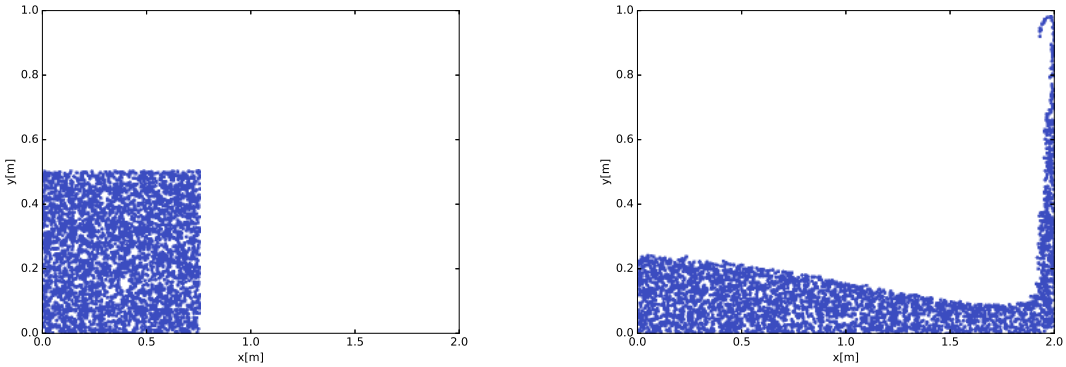

(a) Schematization of dam break problem at $t = 0$ s. (b) Simulation of dam break problem at $t = 0.75$ s.

Figure 3.1: Simulation of dam break problem where the blue dots represent the water particles.

size of domain ($x \times y$)	2 m× 1.5 m
no. of triangular mesh	25 × 15 × 2
size of water body	0.75 m × 0.5 m
particle spacing	0.01 m
time step	0.0075 s
density of water	1000 kg/m^3
density of air	1 kg/m^3
dynamic viscosity	[-] N s/m^2

Table 3.1: Dam break problem - general model setting.

or primarily density jump between two interfaces (air and water). Some of the particles escaping the corresponding mesh can be seen near the left boundary in the figure 3.2a.

The highly viscous fluid cannot collapse totally till the end of simulated time (figure 3.3c) whereas the slightly viscous fluid can propagate and hits the right boundary leading to the dynamic motion of particles (figure 3.2c). Finally the damped motion of water domain is obtained in the case of $\mu = 10^2$ N s/m^2 which depicts the slow motion of the water and shows the steady state. (figure 3.3a). In the figures 3.4a and 3.4b it was approved that this flow indeed leads to the stable (rectangle) shape till $t = 3.75$ s.

3.2.1.2 Functions for increasing viscosity

Although the constant value of viscosity gives rise to damped motion of water particles, the requirement is still that the motions should be damped smoothly for the case of wave simulation. Therefore the second group of simulation was done with the use of various ramp functions.

The hyperbolic tangent functions and exponential functions can represent the smoothly increasing

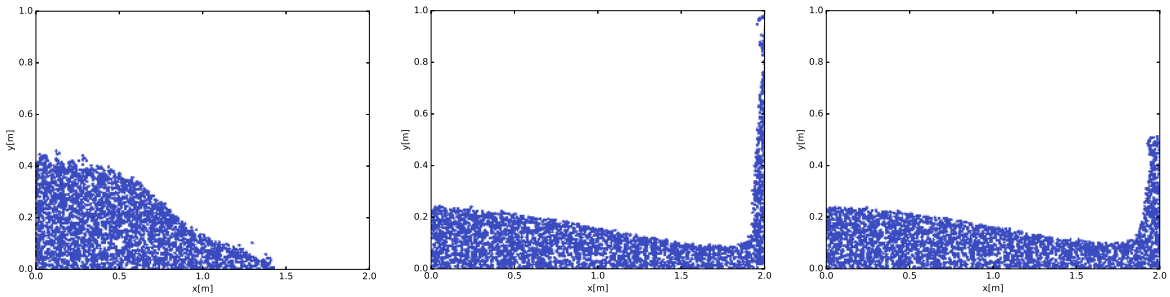

(a) $\mu = 0.1$ at $t = 0.3825$ s. (b) $\mu = 10^0$ at $t = 0.75$ s. (c) $\mu = 10^1$ at $t = 0.75$ s.

Figure 3.2: Dam-break flow using the low viscosity in which the water particles bounce freely within the domain. The loss of the particles occur in figure 3.2a in which the computation was instable.

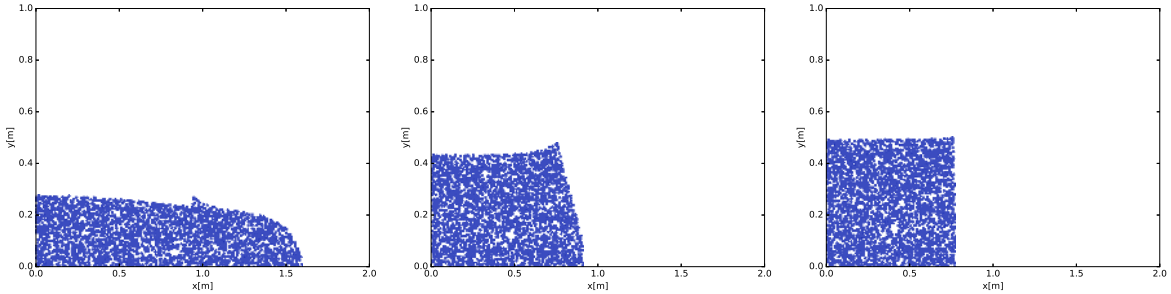

(a) $\mu = 10^2$ at $t = 0.75$ s. (b) $\mu = 10^3$ at $t = 0.75$ s. (c) $\mu = 10^4$ at $t = 0.75$ s.

Figure 3.3: Dam-break flow using high viscosity, causing the water too viscous and rigid to move like the realistic water particles.

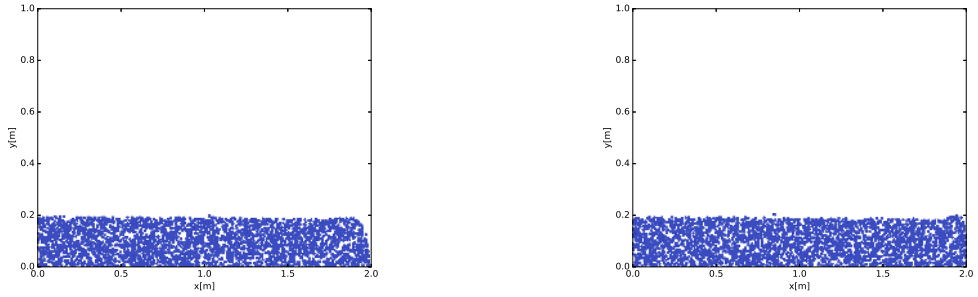

(a) $\mu = 10^2$ at $t = 2.25$ s. (b) $\mu = 10^2$ at $t = 3.75$ s.

Figure 3.4: Dam-break flow using $\mu = 10^2$ which keeps the motion of the water body steady and not violent mode.

viscosity from the start of domain, x_0 to the end of the domain, x_{end}. It is noted that the viscosity should be set to 1 or larger value at x_0 because from the first group of simulation results, the values less than 1 may cause a numerical instability induced by the large density jump.

The tanh functions shown in the figure 3.5a which can produce only up to 4 N s/m^2 for the largest value of viscosity at the end of the computational domain i.e. $x = 2$ m. The figures 3.6a - 3.6c describe that these tanh functions are not suitable for damping of motion. It can be concluded that as long as the viscosity is order of magnitude of 1 in the whole domain, the motion of the flow will not be damped and the water domain also will not be in rigid shape.

Amplification of the tanh function is observed in the figure 3.5b which shows the larger values of viscosity within the small range of domain. The value of function $(\tanh(x)+4.5)^3$ at $x_0 = 0$ shows 91.125 while other curves start from 1 and then increases monotonically. Although the function $(\tanh(x)+4.5)^3$ achieves the steady flow state, this is not desirable one because it does not fulfil the requirement of getting ($\mu = 1$) at $x_0 = 0$.

From the two figures 3.7b and 3.7c, it is observed that the promising function for increasing viscosity is $(20\tanh(x)+1)^2$ which can provide a larger viscosity value very quickly even at $x_0 = 0$. because the dam break flow in the figure 3.7b is in rigid motion till the end of simulation, while the function $(\tanh(x-2)+2)^6$ could not realize the damping of the motion. It also indicates that the maximum viscosity of order of magnitude 1 does not guarantee the force or energy damping. It is confirmed that in order to suppress the dynamic situation of the flow, the viscosity should be at least of order of magnitude 2 for gravity driven flow.

Another candidate for increasing function is exponential function, e^{ax} where a is positive integer, which can provide 1 for the starting value of viscosity at x_0. The parameter a tells the rate of how fast the function increases (figure 3.8a). The function e^{4x} depicts the similar flow state as $(20\tanh(x)+1)^2$ does (figure 3.9b), whilst the e^{10x} produces the extremely viscous fluid, and over-damping condition (figure 3.9a). The difference between these two functions can be easily recognized in the figure 3.8b observing

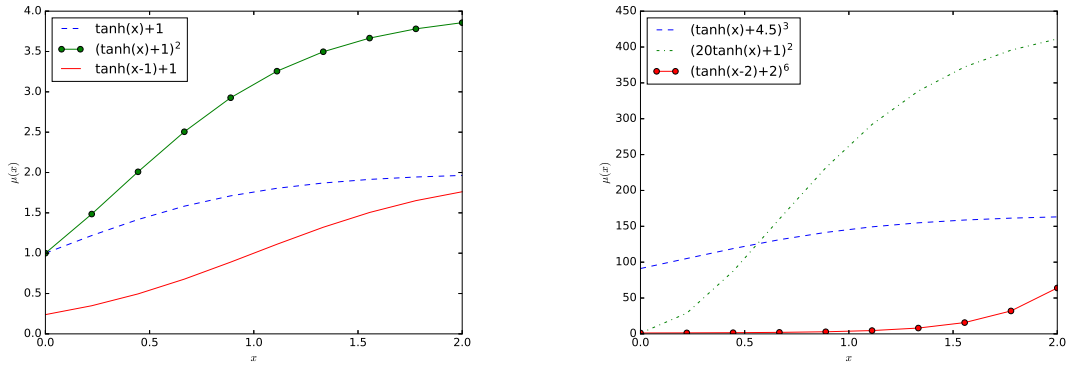

(a) Hyperbolic tangent functions. (b) Hyperbolic tangent functions.

Figure 3.5: The smoothly increasing functions for viscosity which can be implemented in the numerical wave tank or dam break problem. Some of these functions start from $\mu = 0$ while others start from larger vicosity.

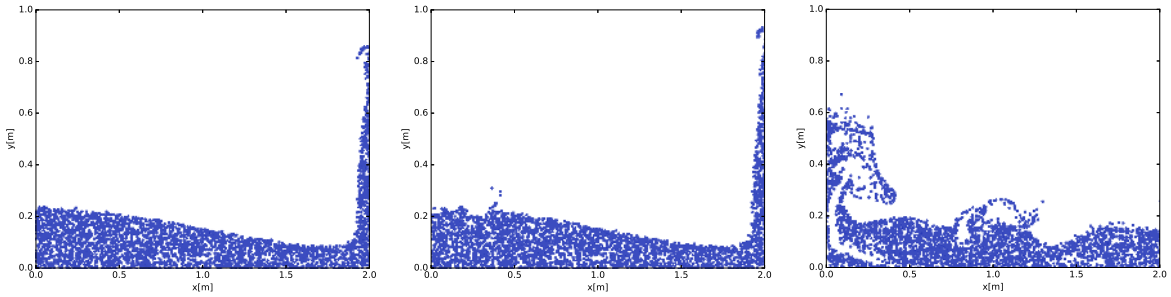

(a) $\mu = \tanh(x)+1$ at $t = 0.75$ s. (b) $\mu = \tanh(x-1)+1$ at $t = 0.75$ s. (c) $\mu = (\tanh(x)+1)^2$ at $t = 2.25$ s.

Figure 3.6: Dam-break flow using ramp function of viscosity that the motion of the water particles could not be damped out.

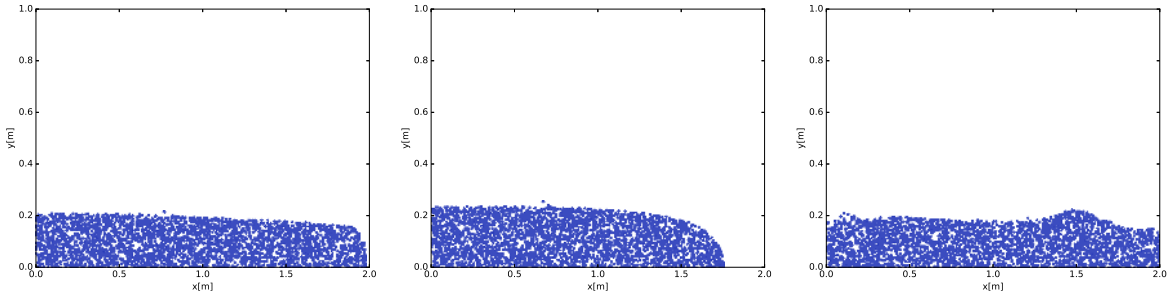

(a) $\mu = (\tanh(x)+4.5)^3$ at $t = 3.75$ s. (b) $\mu = (20\tanh(x)+1)^2$ at $t = 3.75$ s. (c) $\mu = (\tanh(x-2)+2)^6$ at $t = 3.75$ s.

Figure 3.7: Dam-break flow using higher-order ramp function of viscosity in which the steady and calm motion of water body is achieved.

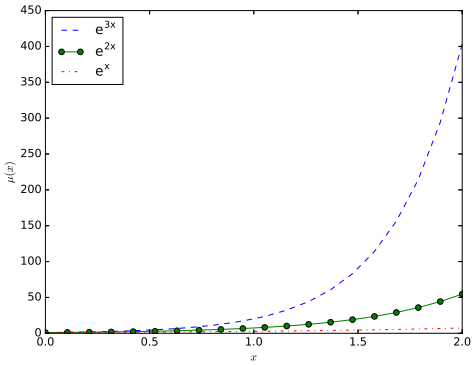

(a) Monotonically increasing functions.

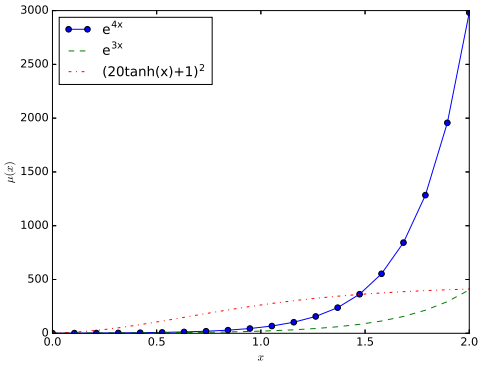

(b) Monotonically increasing functions.

Figure 3.8: Damping functions of which the shape is smoothly increasing without abrupt change in property.

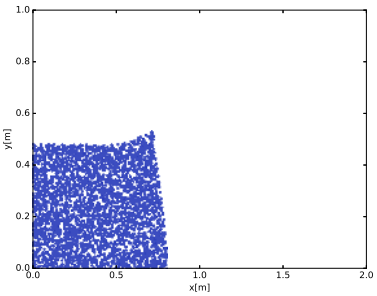

(a) $\mu = e^{10x}$ at $t = 3.75$ s.

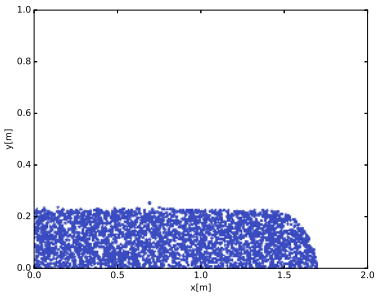

(b) $\mu = e^{4x}$ at $t = 3.75$ s.

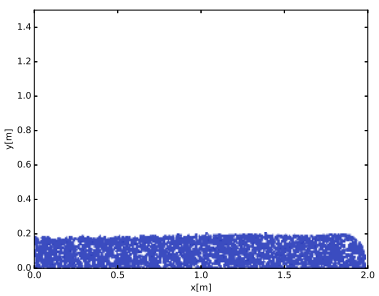

(c) $\mu = e^{3x}$ at $t = 3.75$ s.

Figure 3.9: Dam-break flow in which the exponential function of viscosity was applied.

their ultimate values of viscosity, μ_{end} at $x = 2$ m.

The functions $(20\tanh(x)+1)^2$ and e^{3x} came to the same maximum viscosity at $x = 2$ m although their profiles or rate of progress differ enormously. The obvious point is at $x = 1.5$ where the exponential function could provide only $\mu = 90.01$ N s/m^2 while the tanh function already attained $\mu = 364.92$ N s/m^2. It is therefore confirmed that the flow rate of dam break is faster in case of exponential function (figure 3.9c) than the rate of tanh function application (figure 3.7b).

Another interesting question came out asking how the tanh function modified in terms of cutting off at some points (figure), can serve the requirement of damping motion. The damped motions of water particles described in the figure 3.10b and 3.10c are achieved by the following piecewise functions consisting of tanh function and exponential function respectively as shown in the figure 3.10a:

$$\mu(x) = \begin{cases} 1 & \text{if } x \le 0.5 \\ (20\tanh(3(x-0.5))+1)^2 & \text{if } 0.5 < x \le 1.5 \\ 441 & \text{if } x > 1.5 \end{cases} \tag{3.6}$$

and

$$\mu(x) = \begin{cases} 1 & \text{if } x \le 0.5 \\ e^{4x} & \text{if } 0.5 < x \le 1.5 \\ 404 & \text{if } x > 1.5 \end{cases} \tag{3.7}$$

From the observations explained above, it can be inferred that the most attractive function for increasing viscosity is the customized hyperbolic tangent function with cutting shape (equation 3.6) to dampen the energy smoothly. This function also has the property of conserving the constant value of viscosity ($\mu = 1$) for some spatial distance and then rising to higher value, implying that the over-damping and abrupt transition can be avoided.

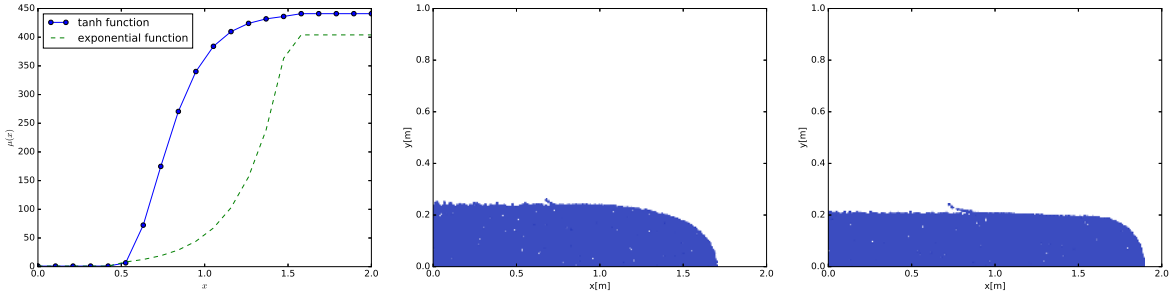

(a) Modified functions. (b) customized tanh at $t = 3.75$ s. (c) exponential at $t = 3.75$ s.

Figure 3.10: Dam-break flow with the modified function of viscosity which was found also applicable.

Generally expressed the generic formulation of the ramp function, it should be as follows:

$$\mu(x) = \begin{cases} I & \text{if } x < \frac{1}{4}L \\ \left(A \tanh\left(S\left(x - \frac{1}{4}L\right)\right) + \sqrt{I}\right)^2 & \text{if } x \geq \frac{1}{4}L \end{cases} \tag{3.8}$$

where I is the initial viscosity value defined by the property of the fluid. The parameter A denotes the amplification factor which amplifies the function value significantly which is especially useful for shorter computational domain because it gives rise to larger value quickly within the short length of sponge layer generally. The parameter S is defined as the slope parameter which determines if the slope of the function is mild or steep. Although the extreme steep slope rises to the higher damping viscosity in shorter time, it results in the partial reflection which will be explained in the section 4, because the fluid behaves like a rigid body suddenly at that point. Using the mild slope of the function makes the gentle damping, however it causes longer computational domain, leading to the waste of computational power. The term $\frac{1}{4}L$ is the shift in function where the viscosity value starts to increase from the constant value, $\mu = 1$.

3.2.2 Conclusion

The effect of different constant values of the viscosity on the motion of the water body was assessed using the dam break problem. Moreover a variety of viscosity functions is implemented in the dam break model for the assessment of spatial varying viscosity in the domain. The most attractive function for damping the motion of the water particles is the hyperbolic tangent function. The function can also be modified as necessary e.g. shifting the spatial coordinates, the slope of the function and amplification of the function.

Chapter 4

Wave Generation and Absorption

In this section, the generation of waves in the NWT are discussed following the section of boundary conditions. The generation of solitary waves and linear progressive waves were simulated using the different computational settings for the benchmark test. The wave absorption in the NWT is also studied using the relaxation approach or sponge layer approach which applies the highly viscous materials for dissipation of waves (2.2.3). The following two aspects will be considered mainly regarding the accuracy of the solution:

1. Density mapping from the particles to the grid system
2. Boundary condition which controls the property of the generated wave

4.0.1 Boundary Conditions

Among the methods for wave generation in the NWT explained in the literature review 2.2, the wave paddle approach (2.2.3) which is the most similar to the realistic wave plate is used in the present research. Furthermore, as the moving boundary approach, the cells which are assigned as boundary condition will be moving according to the displacement function $X(t)$ of the wave plate derived from the linear wavemaker theory.

The non-homogeneous Dirichlet boundary condition will be enforced to drive the wavemaker. The setting of different boundary conditions are depicted in the figure 4.1. The left boundary is the moving boundary assigned by the velocity function $v(t) = \frac{dX(t)}{dt}$ of the wave plate.

4.1 Benchmark test: Solitary waves generation

The application of solitary waves or solitons in the NWT is a traditional approach for validation of capability of a newly developed numerical method. The soliton is a non-linear wave in which the single humped of bulge of water mass can propagate with high stability of shape and speed, discovered experimentally by Russell (1844) (Wazwaz 2010). The approximate solution for the surface elevation of the solitary wave accurate to the order $\left(\frac{H}{d}\right)^2$ is given by the equation 4.1 (Mei et al. 1989):

$$\zeta = H\mathrm{sech}^2\left[\sqrt{\frac{3}{4}\frac{H}{d^3}}(x-ct)\right] \tag{4.1}$$

in which H is the wave height, d is the undisturbed water depth and $c = \sqrt{g(d+H)}$ is the wave celerity where g is the gravitational acceleration.

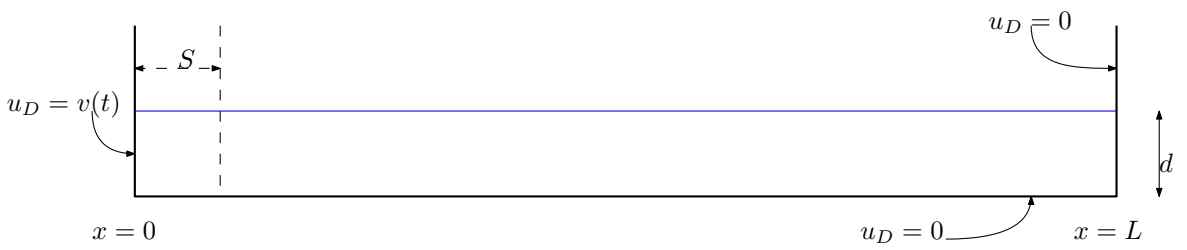

Figure 4.1: Numerical wave tank

size of domain ($x \times y$)	10 m× 0.6 m
no. of triangular mesh	200 × 12 × 2
size of water body	10 m × 0.3 m
particle spacing	0.0065 m
time step	0.01 s
density of water	1000 kg/m^3
density of air	1 kg/m^3
dynamic viscosity	1 N s/m^2

Table 4.1: Solitary wave generation - general model setting

4.1.1 Boundary movement

The boundary movement function for solitary wave generation pioneered by Goring (1978) is applied here. Maljaars (2016) modified the paddle law of motion of previous researchers to realize the correct movement:

$$X(t) = S \tanh\left[7.6\left(\frac{t}{\tau} - \frac{1}{2}\right)\right] + S \tag{4.2}$$

$$v(t) = S\frac{7.6}{\tau}\text{sech}^2\left[7.6\left(\frac{t}{\tau} - \frac{1}{2}\right)\right] \tag{4.3}$$

where S is stroke of the paddle and τ is the duration of the paddle, defined by the equations below respectively:

$$S = 2\sqrt{\frac{Hd}{3}} \qquad \text{and} \qquad \tau = \frac{4}{\beta c}\left(\tanh^{-1}(0.999) + \frac{H}{d}\right)$$

where β denotes the outskirt decay coefficient given by:

$$\beta = 2\sqrt{\frac{3H}{4d^3}}$$

4.1.2 Simulation results

Recapping the main idea of the research, there exist two objectives for the simulation of solitary wave generation. These two objectives are as follows:

1. To compare the wave profile of the simulated soliton against the analytical profile in terms of the absolute wave celerity and the relative wave crest position, and
2. To observe the damping of the solitary wave using various viscosity functions placed near the right side of the computational domain

4.1.2.1 Generation of solitary waves

The comparison of wave profile was done for four relative wave heights using the setting from the table 4.1. The waves are simulated for 600 time steps i.e till 6 s. In the figure 4.2a for relative wave height $\frac{H}{d} = 0.2$ the analytical wave profile in white colour matches the simulated blue-coloured wave profile almost exactly while in other three figures 4.2b-4.2d these two wave shapes do not overlap each other. This proves that the wavemaker theory used in this simulation is only valid for utmost $\frac{H}{d} \leq 0.2$ (Mei et al. 1989).

For larger wave heights (figures 4.2b-4.2d), the analytical wave shape is lag behind the simulated wave. Although the analytically calculated wave celerity is approximately close to the visually calculated wave celerity, the position of their wave crests are slightly different. For instance, to calculate the analytical velocity of the solitary wave for $\frac{H}{d} = 0.35$, the formula $c_{\text{analy}} = \sqrt{g(H+d)}$ gives the value of $c_{\text{analy}} = \sqrt{9.81(0.105+0.3)} = 1.99$ m/s. The velocity of the simulated soliton can be obtained using the figures 4.4, it turns out to be $c_{\text{sim}} = \frac{3.6-1.6}{1} = 2$ m/s. It also should be noted that the trailing part of the soliton in each simulation has the deficit shape unlike the perfect wave profile. It is the well-known observation of many previous solitary wave simulations.

If each of these four simulations were analysed again in detail, in the case of relative wave height

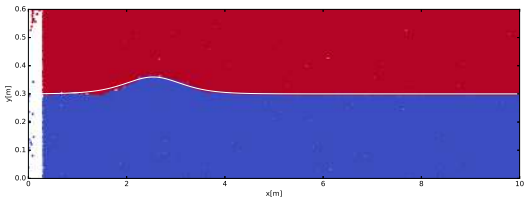

(a) Relative wave height $\frac{H}{d} = 0.2$.

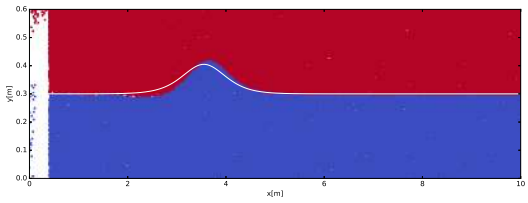

(b) Relative wave height $\frac{H}{d} = 0.35$.

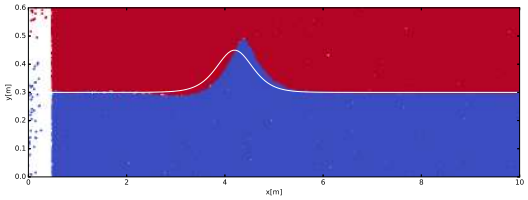

(c) Relative wave height $\frac{H}{d} = 0.5$.

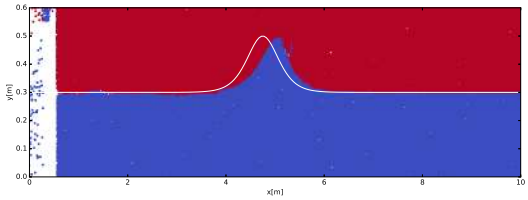

(d) Relative wave height $\frac{H}{d} = 0.67$.

Figure 4.2: Analytical and Simulated wave profiles for different relative wave heights in which the white line denotes the analytical wave profile. Each of these cases are studied in detail later.

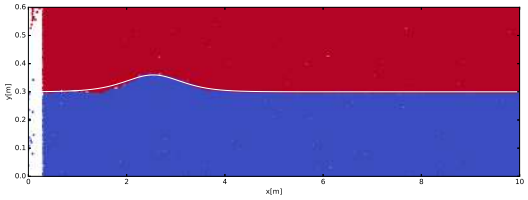

(a) Relative wave height $\frac{H}{d} = 0.2$ at $t = 3$ s.

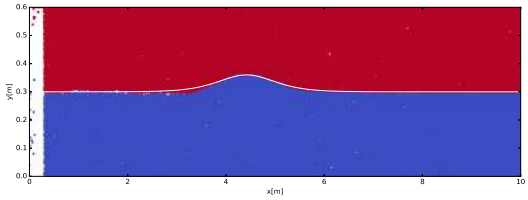

(b) Relative wave height $\frac{H}{d} = 0.2$ at $t = 4$ s.

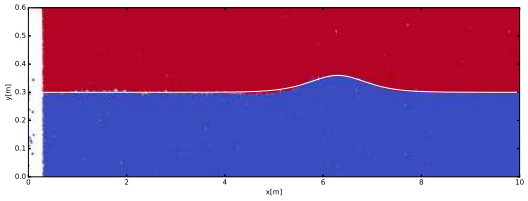

(c) Relative wave height $\frac{H}{d} = 0.2$ at $t = 5$ s.

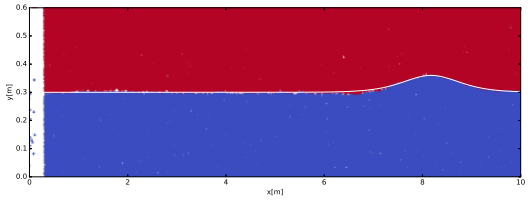

(d) Relative wave height $\frac{H}{d} = 0.2$ at $t = 6$ s.

Figure 4.3: Comparison of analytical and simulated amplitudes for $\frac{H}{d} = 0.2$ which shows the exact match between them. The amplitude and phase of these solutions coexist for each second. The white line is the analytical solution while the blue and red color areas are the water and air domain respectively. These notations will hold the same for each case.

$\frac{H}{d} = 0.2$ the numerical amplitude and analytical amplitude show the same magnitude and in phase while propagating as depicted in the figures 4.3.

Since for the relative wave height $\frac{H}{d} = 0.35$ a discrepancy between the phase of the analytical soliton and simulated soliton was observed as mentioned earlier, a small shift in the time frame in the analytical solution was done in order to check if any discrepancy still remains or not. The shift was implemented in time by 0.075 s to move the crest position of the soliton in the right direction. The figures 4.4 prove that the shifting in time does not cause the analytical solution lag behind the simulated one at every time step.

However in the simulations of larger relative wave height, it should be noted that the amplitude of the simulated solution is slightly larger than the analytical one, because the water particles in the deficit wave trough seem to accumulate in the wave crest. This is in accordance with the opinion of Wu et al. (2014) on the physical solitary waves in the EWT using the Goring (1978)'s approach. On the other hand, the noticeable observation in the figures 4.4 is that after every time step the amplitude of the former one gradually decreases to match that of the latter one, i.e. the simulated waves decay as the time continues. The simulation of Wu et al. (2014) also confirms this phenomenon of a solitary wave decay.

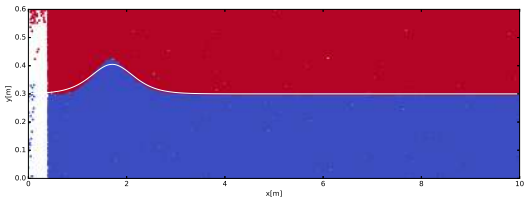

(a) Relative wave height $\frac{H}{d} = 0.35$ at $t = 2$ s.

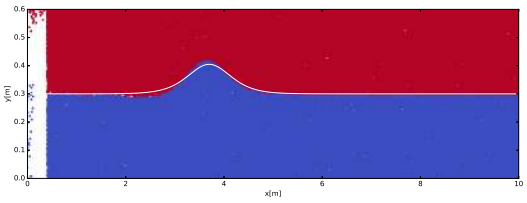

(b) Relative wave height $\frac{H}{d} = 0.35$ at $t = 3$ s.

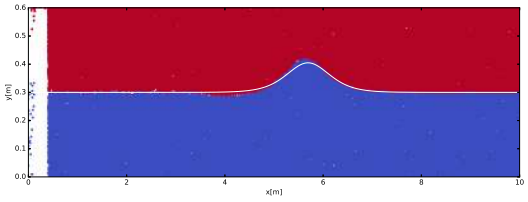

(c) Relative wave height $\frac{H}{d} = 0.35$ at $t = 4$ s.

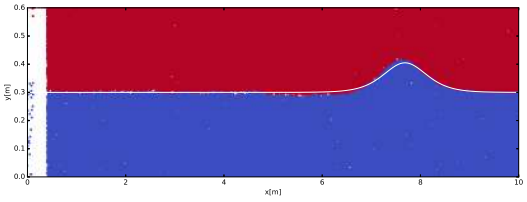

(d) Relative wave height $\frac{H}{d} = 0.35$ at $t = 5$ s.

Figure 4.4: Comparison of analytical and simulated amplitudes for $\frac{H}{d} = 0.35$ where the former one is lagging behind the latter one originally, but in the figures 4.4a-4.4d a small time shift of 0.075 s was done in the analytical solution to match these two solutions.

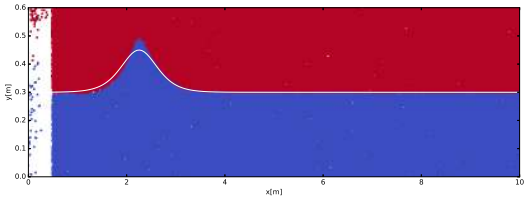

(a) Relative wave height $\frac{H}{d} = 0.5$ at $t = 2$ s.

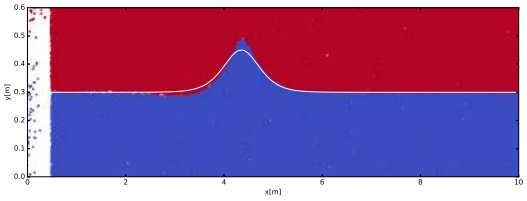

(b) Relative wave height $\frac{H}{d} = 0.5$ at $t = 3$ s.

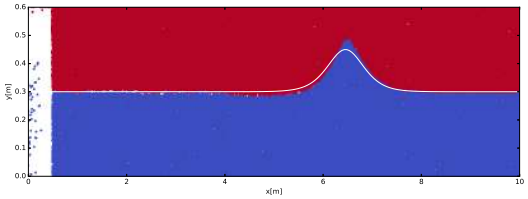

(c) Relative wave height $\frac{H}{d} = 0.5$ at $t = 4$ s.

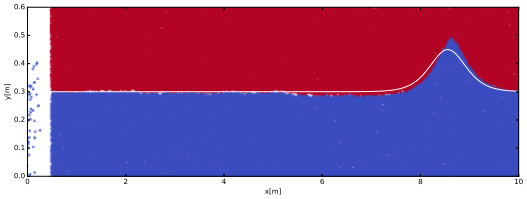

(d) Relative wave height $\frac{H}{d} = 0.5$ at $t = 5$ s.

Figure 4.5: Comparison of analytical and simulated amplitudes for $\frac{H}{d} = 0.5$ where the same process was observed as the relative wave height $\frac{H}{d} = 0.35$ (figures 4.4). The simulated wave amplitude became diffuse as it propagates.

Again using the same time shift of 0.075 s in the simulations of $\frac{H}{d} = 0.5$ and $\frac{H}{d} = 0.67$, it was observed that their wave profiles match apparently in each second. In the figure 4.5d, however, the simulated soliton propagates faster than the analytical one again at $t = 5$ s. The same investigation was shown in the figures 4.6 but in that case because of the larger relative wave height the wave breaking occurs after a few seconds of the simulation. Actually their relative wave heights exceed the validity of the generation of solitary waves of $\frac{H}{d} = 0.2$ which will use the equation 4.3, so the generated solitons are not accurate.

In order to assess the difference between the three projection methods for mapping the density from the particles to the grid, three simulations were done using these methods for $\frac{H}{d} = 0.35$:

1. Standard least square mapping
2. Bounded such that $\rho_a \leq \rho \leq \rho_w$
3. Constrained such that $\nabla \times (\rho \mathbf{f}) = 0$

These three projections lead to the different effects on the interface between air and water, in other words the density jump between the two phases. The simulation of method 1 failed at time $t = 1$ s because of severe discontinuity in left side of the interface (figure 4.7b) i.e the water particles in the water surface

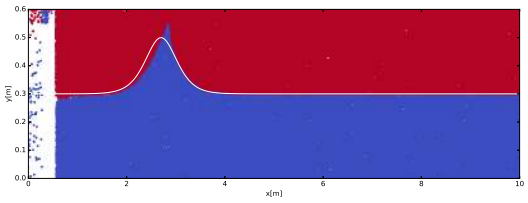

(a) Relative wave height $\frac{H}{d} = 0.67$ at $t = 2$ s.

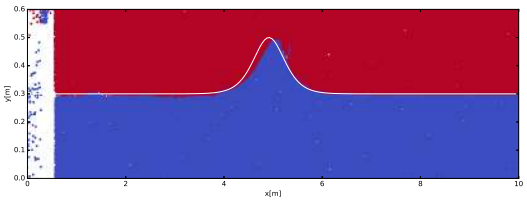

(b) Relative wave height $\frac{H}{d} = 0.67$ at $t = 3$ s.

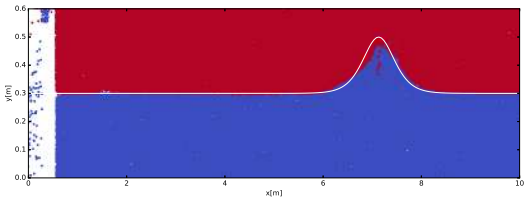

(c) Relative wave height $\frac{H}{d} = 0.67$ at $t = 4$ s.

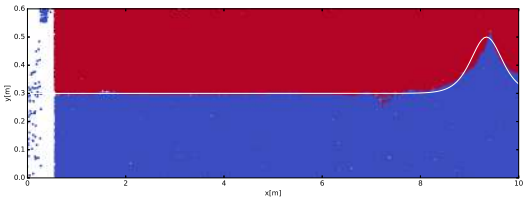

(d) Relative wave height $\frac{H}{d} = 0.67$ at $t = 5$ s.

Figure 4.6: Comparison of analytical and simulated amplitudes for $\frac{H}{d} = 0.67$ where the wave breaking occurs due to the large relative wave height.

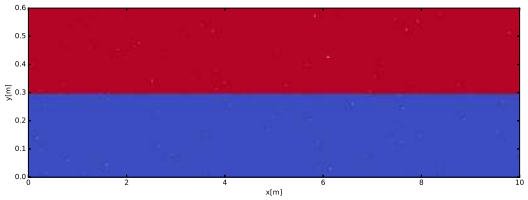

(a) Method 1 for $\frac{H}{d} = 0.35$ at $t = 0$ s.

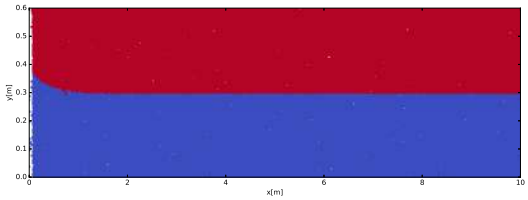

(b) Method 1 for $\frac{H}{d} = 0.35$ at $t = 1$ s.

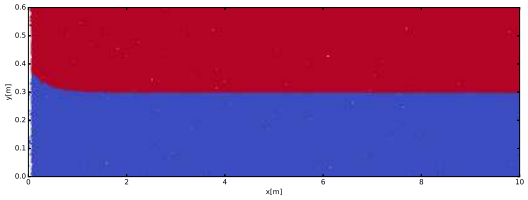

(c) Method 2 for $\frac{H}{d} = 0.35$ at $t = 1$ s.

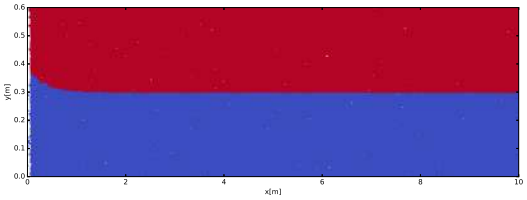

(d) Method 3 for $\frac{H}{d} = 0.35$ at $t = 1$ s.

Figure 4.7: Interface between air and water phases for $\frac{H}{d} = 0.35$ due to different density mapping from the particles to the mesh. Method 1 failed to continue the computations while the rest two method provide barely visible difference in surface profile.

are out of the mesh too far to cope with. The other two methods could handle the simulation till the end without any failure though the figures 4.7c and 4.7d at $t = 1$ s are shown for mere comparison purposes.

4.1.2.2 Absorption of solitary waves

To demonstrate the wave absorption in the NWT, the case of $\frac{H}{d} = 0.2$ was simulated in 15 m long flume with the customized hyperbolic tangent function. The applicability of this function for viscous damping has been proved in the section 3. It should be kept in mind that an abrupt change of viscosity does give rise to wave reflection at that transition point as it acts as a rigid body. In order to guarantee the wave absorption via viscous damping, the smooth shape of viscosity function should be implemented in the NWT as described in the figure 4.8. Such a long flume is required to accommodate this damping function in such a way to dampen the waves nicely without reflection back into the wave generation region.

The function in the figure 4.8 reads as follows:

$$\mu(x) = \begin{cases} 1 & \text{if } x \leq 6 \\ (30\tanh(x-6)+1)^{1.5} & \text{if } 6 < x \leq 10 \\ 172.432 & \text{if } x > 10 \end{cases} \tag{4.4}$$

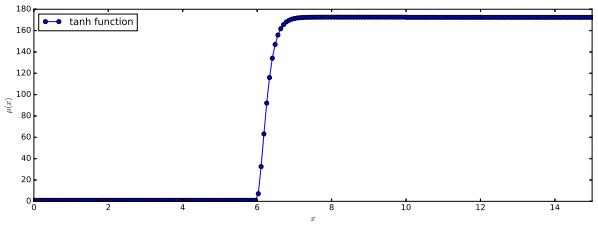

Figure 4.8: Customized hyperbolic tangent function.

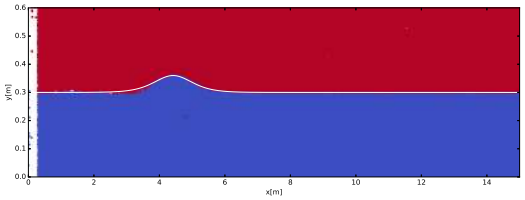

(a) Propagation of soliton at $t = 4$ s.

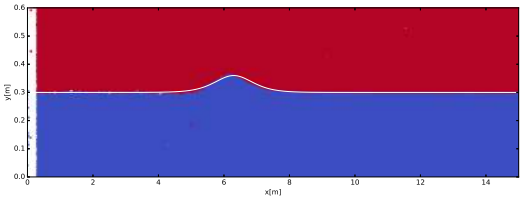

(b) Propagation of soliton at $t = 5$ s.

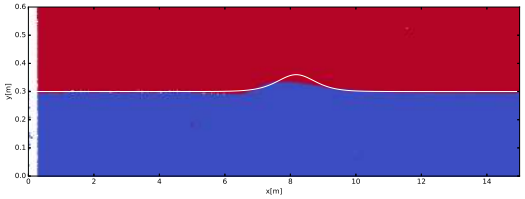

(c) Propagation of soliton at $t = 6$ s.

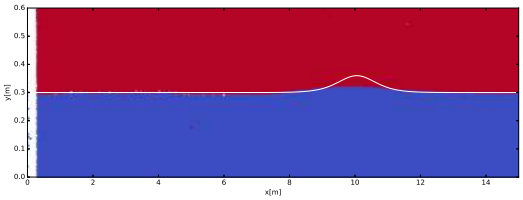

(d) Propagation of soliton at $t = 7$ s.

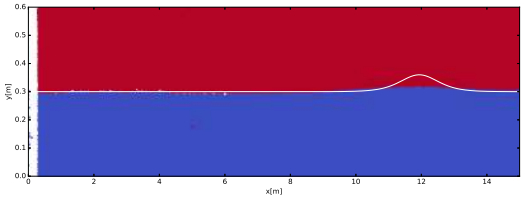

(e) Propagation of soliton at $t = 8$ s.

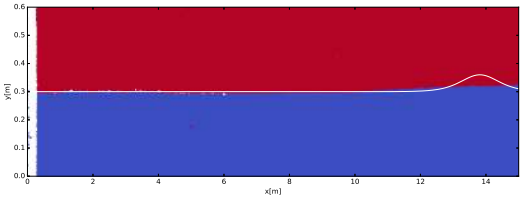

(f) Propagation of soliton at $t = 9$ s.

Figure 4.9: Absorption of soliton $\left(\frac{H}{d} = 0.2\right)$ where the viscous function of equation 4.4 was implemented in the flume and the wave are apparently damped out. However due to the continuity of water mass in a closed flume, the particles accumulate near the right side of the tank, leading to the rise of surface elevation slightly.

On the other hand, due to the consideration of computational expensiveness for a long NWT, even though the very slowing increasing viscosity function is desirable for perfect absorption, the optimal shape of function is more practical as in the figure 4.8. The figures 4.9 indeed exhibit the satisfactory results of wave absorption using the customized hyperbolic tangent function. The water surface elevation shows a slightly small slope near the right portion of the NWT because of the continuity of water mass in the tank. The while coloured line is shown for analytical wave profile to observe the damping phenomenon clearly.

Another simulation which uses the relative wave height $\frac{H}{d} = 0.2667$ was done in order to study the effectiveness of the damping function shown in the figure 4.8, looking at whether the larger solitary wave will be damped out or not. Although the small shift of 0.07 s was needed for matching the analytical and simulated wave profiles, the soliton has damped eventually, keeping the rise of water surface slope as before. The figures are shown in the appendix.

In fact, the successful wave absorption was attained after a handful of simulations using the short NWTs and other viscosity functions e.g exponential function. In these cases, the partial reflection was observed due to the failure of viscosity function, for instance, the function value reaching the large viscosity in a short distance. The examples are obvious in the figures 4.10 showing abnormal oscillations.

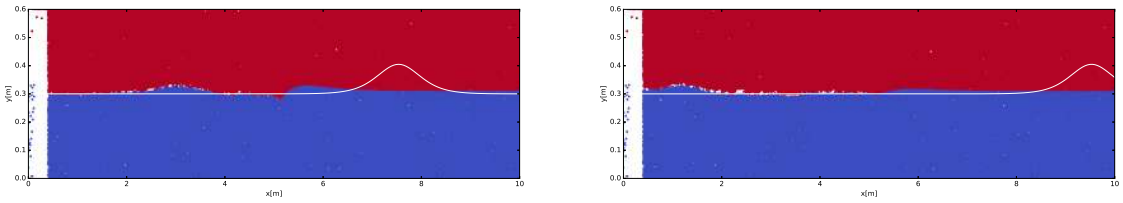

(a) Propagation of soliton for $\frac{H}{d} = 0.35$ at $t = 5$ s. (b) Propagation of soliton for $\frac{H}{d} = 0.35$ at $t = 6$ s.

Figure 4.10: Partial reflection of soliton due to abrupt change of viscosity.

4.1.3 Conclusion

1. The present numerical method could work for solitary wave generation of the relative wave height $\frac{H}{d} = 0.2$ in terms of matching the analytical and numerical wave celerity and their wave crest positions. Regarding the projection method for mapping the mesh system to the particles, the method 2 and method 3 does not give rise to sharp differences.

2. The satisfactory wave absorption was carried out in the extended NWT with the use of the customized function. The drawback of this approach is the rise of water surface slope near the end of the tank due to water mass conservation inside the closed volume. Strangely the computation was hanging at time step 971 or $t = 9.71$ s.

3. The general formulation for the damping function can be drawn as follows:

$$\mu(x) = \begin{cases} I & \text{if } x \le x_1 \\ \left(A \tanh(S(x - x_1)) + \sqrt{I}\right)^D & \text{if } x_1 \le x \le L \end{cases} \tag{4.5}$$

   where I is the initial value of the viscosity which can be the intrinsic property of the fluid, x_1 is the starting point of the sponge layer, $x - x_1$ is the spatial length where the wave simulation will be studied, A is the amplification factor, S is the slope parameter, and D is the power factor. The parameters A and S have the quality as same as explained in the dam-break flow case (section 3). The power factor D is useful for a quick enlargement of the damping function within the size limitation of the computational domain.

   The maximum value of this function should be the order of magnitude $\sim 10^2$. The most important factor is the slope parameter S because it can prevent the sudden change of fluid property. It also determines the length of the sponge layer so it should be of order of magnitude $\sim 10^0$.

   The length of the damping zone is also dependent on the wave properties of the soliton because the energetic wave requires longer dissipation zone than the moderate wave. For the case of $\frac{H}{d} = 0.2$, the damping zone of 9 m length was required to absorb the waves. Another requirement is in order to prevent the large surface slope after wave absorption, the damping zone should be long enough to accommodate the wave. It can be deduced that the length of the damping zone is not a function of that of the wave flume, but a function of the wavelength.

4. Following the above conclusion, it should be said that there are two constraints for determining the parameters of the damping function. These two constraints are (1) to obtain a smoothly increasing function within a short sponge layer, and (2) to acquire which maximum value of viscosity should be provided in this range of damping zone. These two factors are indeed competing each other due to the ultimate restriction of saving computational power.

5. In fact, this absorption technique does not dissipate the wave amplitude totally, however it enhances the wave to be in diffusive manner, leading to the rising of the water surface slope. For longer simulation time, that phenomenon can cause undesirable consequences in the wave tank.

4.2 Benchmark test: Progressive wave generation

The linear progressive waves are also studied for the validation of the NWT using the hybrid particle-mesh method. Due to the complexity of mathematical formulation for the Cnoidal wave generation (Cho 2003), in this simulation only the linear progressive waves are chosen to be investigated for the sake of simplicity.

size of domain ($x \times y$)	8 m× 0.6 m
no. of triangular mesh	200 × 15 × 2
size of water body	8 m × 0.4 m
particle spacing	0.0055 m
time step	0.01 s
density of water	1000 kg/m^3
density of air	1 kg/m^3
dynamic viscosity	2.5 N s/m^2

Table 4.2: Progressive wave generation - general model setting.

The analytical solution for the surface elevation of the progressive wave is as the following (Dean and Dalrymple 1991):

$$\eta = \frac{H}{2}\cos(kx - \sigma t) \qquad \text{for } x >> h \tag{4.6}$$

where H is the wave height, $k = \frac{2\pi}{L}$ is the wavenumber, h is the water depth and σ is angular frequency. However this equation 4.6 should be used to validate the waves which are far away from the wave paddle by means of multiple times the water depth in the NWT.

4.2.1 Boundary movement

Following the formulation of Dean and Dalrymple (1991) for the wave generation in the EWT, the movement of the piston type wave paddle is defined as below:

$$X(t) = \frac{S}{2}\sin(\omega t) \tag{4.7}$$

$$v(t) = \frac{S}{2}\omega\cos(\omega t) \tag{4.8}$$

where S denotes the stroke of the wave paddle, and ω is the wavemaker frequency. Also the paddle stroke S is given by:

$$S = A\frac{2kh + \sinh(2kh)}{\cosh(2kh) - 1} \tag{4.9}$$

where A is the amplitude of the required wave at a distance (say $x > 3h$) from the wavemaker, k is the wavenumber $\left(k = \frac{2\pi}{L}\right)$, L is the wavelength and h is the water depth. Here it should be noted that this linear first-order wavemaker theory was devised assuming that the generated wave heights are small and the amplitude of the wave paddle motion is small as well. Moreover, the aforementioned wave paddle movement equations 4.8 are valid only for the shallow water waves $\left(\frac{L}{h} > 20\right)$ (Dean and Dalrymple 1991).

4.2.2 Simulation results

The two objectives set up in the solitary wave section 4.1.2 will be targeted again here. These are described briefly: (1) the comparison of analytical and simulated wave profiles, and (2) the damping of linear (small-amplitude) progressive waves via passive absorption. It should be noted that the analysis of using three different mapping procedures are not repeated in this part, since it has been noticed that method 2 and method 3 gives very similar surface profiles which was already proved in the section 4.1.2. Eventually the method 2 was applied in this generation of progressive waves.

4.2.2.1 Generation of linear progressive waves

The general model setting is shown in the table 4.2, as the particle spacing and grid sizes may change according to the length scale of the wave properties. Although the equations 4.8 are designated for shallow water waves, here we will simulate three waves for deep water, intermediate water, and shallow water respectively in order to validate the first-order linear wavemaker theory. The waves are simulated for a duration of 10 s except for the deep water waves for the reason explained later.

The figures 4.11a and 4.11b show that the NWT failed to simulate the short waves or deep water waves because of incompatible wavemaker equations, since the equations 4.8 are derived for long waves or shallow water waves. It was found that the simulated short waves could not propagate in the tank as the time proceeds from 2 s to 3 s. Therefore the simulation was stopped at that instance since the

	Deep water $\left(\frac{h}{L} > 0.5\right)$	Intermediate water $\left(0.05 < \frac{h}{L} < 0.5\right)$	Shallow water $\left(\frac{h}{L} < 0.05\right)$
water depth	0.4 m	0.4 m	0.2 m
wavelength	0.316165 m	1.4637 m	4.13942 m
amplitude	0.04 m	0.04 m	0.04 m
size of domain	8 m × 0.6 m	8 m × 0.6 m	8 m × 0.4 m
wave period	0.45 s	1 s	3 s

Table 4.3: Linear progressive waves.

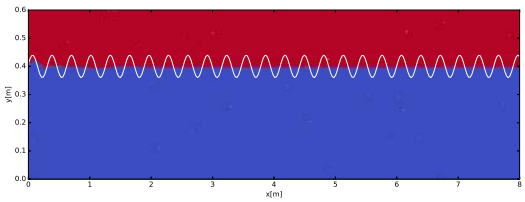

(a) Deep water waves $\frac{h}{L} = 1.26$ at $t = 2$ s.

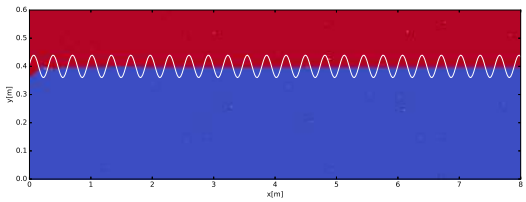

(b) Deep water waves $\frac{h}{L} = 1.26$ at $t = 3$ s.

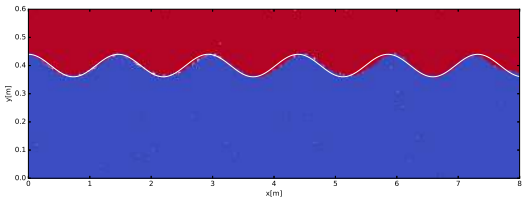

(c) Intermediate water wave $\frac{h}{L} = 0.273$ at $t = 9$ s.

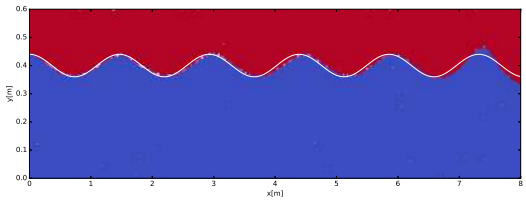

(d) Intermediate water wave $\frac{h}{L} = 0.273$ at $t = 10$ s.

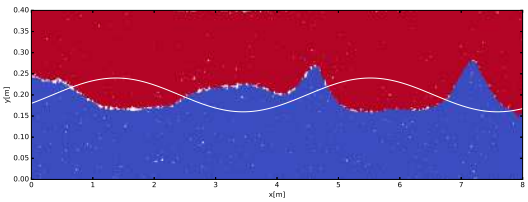

(e) Deep water wave $\frac{h}{L} = 0.0483$ at $t = 9$ s.

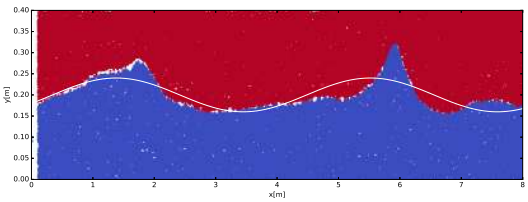

(f) Deep water wave $\frac{h}{L} = 0.0483$ at $t = 10$ s.

Figure 4.11: Comparison of analytical and simulated profiles for wave properties in the table 4.2 in which the intermediate water waves could be simulated very accurately while the deep water waves and very long waves are failed to simulate.

size of domain ($x \times y$)	12 m× 0.12 m
no. of triangular mesh	800 × 12 × 2
size of water body	12 m × 0.08 m
particle spacing	0.002 m
time step	0.01 s
viscosity	viscous function (equation 4.4)
wave amplitude	0.01 m
wave period	2 s

Table 4.4: Progressive wave generation - Long wave.

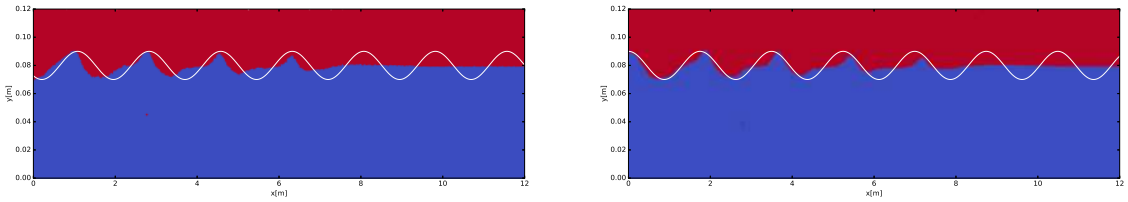

(a) Shallow water waves $\frac{h}{L} = 0.$ at $t = 9$ s.

(b) Shallow water waves $\frac{h}{L} = 0.273$ at $t = 10$ s.

Figure 4.12: Comparison of analytical and simulated profile for wave property in the table 4.4 where the generated wave profiles are skewed in both x and z directions. The strange observation is that even thought the wavemaker equations are designed for generation of long waves, in practice it failed up to 10 sec in the 15 m flume.

longer simulation is not necessary any more. However the intermediate water waves are well captured after some periods in the NWT as depicted in the figures 4.11c and 4.11d. In this case the wave reflection can be seen in the figure 4.11d, making the wave profile deform at the right boundary of the tank.

For long wave of $L = 4.14$ m, the short wave tank could not accommodate it enough to capture at all because of reflection at the termination which happens within a very short time, unlike the previous cases. This can be observed in the figures 4.11e and 4.11f which describe the violent wave profile. This leads to another simulation of long wavelength $L = 1.747$ m using an extended long flume of 15 m.

The new setting of the long wave simulation is described in the table 4.4. The figures 4.12a and 4.12b depict the surface profiles of the simulation. Even at 9 s of the simulation, the water surface could not attain the correct sinusoidal shape, induced by the skewness (figure 4.12a). However the leading face of the wave is in agreement of that of the analytical profile, whereas this is not the case for the lagging face (4.12b).

4.2.2.2 Absorption of linear progressive waves

The test case of intermediate water waves was employed for absorption since this test case could provide the most satisfying wave profiles as explained above. However the long wave flume of 15 m is used in order to insert the sponge layer which is as exactly similar configuration as that of solitary wave case 4.1.2. The equation of increasing viscosity function is referred to the equation 4.4 as well.

The figures 4.13a and 4.13b show the surface elevations of the progressive wave affected by the absorption of wave tank. The computation was unstable due to the loss of particles at the time step of 8.75 s. At this instance, the initial wave crest arrived only at 6 m where the viscosity starts to increase, whilst the wave can propagate freely without the absorption scheme (figure 4.11d). The absorption scheme acts apparently as the highly viscous body which resists hugely against the wave propagation, leading to the distortion of surface profile. This phenomenon is obvious in the figure 4.13a where the first wave crest became sharp.

4.2.3 Conclusion

1. The present hybrid particle-mesh method could simulate the intermediate water waves with reliable accuracy using the first order wavemaker equations. The method failed to obtain the successful simulation of the deep water waves and shallow water waves within short range of computational

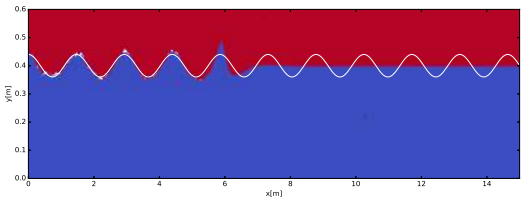

(a) Intermediate water waves $\frac{h}{L} = 0.273$ at $t = 8$ s.

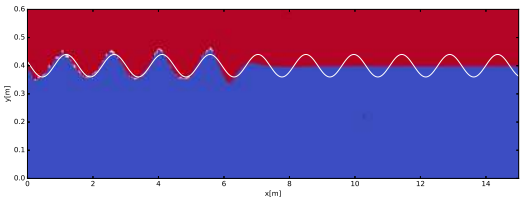

(b) Intermediate water waves $\frac{h}{L} = 0.273$ at $t = 8.75$ s.

Figure 4.13: Absorption of progressive waves at intermediate depth in which the same viscosity function was implemented as the absorption of the solitary wave.

time. This is because the shallow water waves require a long flume to accommodate them without any reflection effect. The simulated short waves cannot travel beyond the wave generation zone because of little amount of energy and wrong usage of the generation equations.

2. The sponge layer approach presented in the section 4.1.2 was implemented to observe the absorption phenomenon of the progressive waves. It could not be concluded whether the waves are absorbed or not at the right side of the wave tank, since the computation breaks down during the simulation period, and then the waves could not propagate anymore.

Chapter 5

Recommendations and Conclusions

In this section, the recommendations and conclusions are drawn for the wave generation and absorption of solitary and linear progressive waves, regarding to the numerical approach and physical approach.

5.1 Solitary wave – Generation and Absorption

1. The generation approach of solitary wave by Goring (1978) is applicable for the waves of up to relative wave height, $\frac{H}{d} = 0.2$ whilst Wu et al. (2014) conducted some modifications in his approach by applying Fenton's solitary solution to get the accuracy for waves of $\frac{H}{d} = 0.4$, using the meshless numerical methods. In the future hybrid particle-mesh method, their modified wave generation method should be included to validate.

2. In this research, due to the restriction of computational power the flumes of only 10 m and 15 m long could be simulated for validation of the wave generation and wave absorption for short simulation time (t=9 s). An extended wave tank should be conducted for longer simulation time to observe the stability of the solitary wave form and the situation after absorption at the right side of the tank.

3. The values of the parameters in the equation 4.5 need to researched more for different range of solitary wave properties. However, the rule of thumb for choosing these values are provided in the section 4.1.3.

4. The computational loading of the simulation is indeed dependent on the spacing of the particles inside each cell, which in turn affects the projection or mapping technique from the particles to the mesh. In order to optimize the computational power for large spacing between the particles, new innovative interpolation methods should be devised for particle projection to the grid.

5. Among the two ways of passive absorption technique mentioned in the section 2.2.4, in the current research the absorption of using internal friction or viscous damping was applied instead of using external pressure via free surface boundary conditions. Since the latter one is intended to use for the potential flow theory originally, here in the real flow case only the former one was implemented. In the future the technique of using free surface boundary condition should be included in the real flow for damping in order to observe the possibility of wave absorption.

6. The Newtonian cooling coefficient should also be added in the governing NS equations to speed up the damping rate and to absorb the different range of wavelengths.

5.2 Progressive wave – Generation and Absorption

1. The suitable wave generation or wavemaker equations should be used for the generation of long waves and short waves, because the wavemaker equations used in the present research can work out only for the waves in the intermediate water.

2. Moreover, for the absorption of the intermediate water waves via the sponge layer approach, a better viscous function should be put to avoid the squeeze of water particles and the instability of the computation.

3. Eventually the alternative approach for the wave absorption should be used, such as active absorption (Shibata et al. 2011), dissipation via the free surface boundary condition (Kim et al. 2014), and Newtonian cooling coefficient (Cao et al. 1993).

Appendix

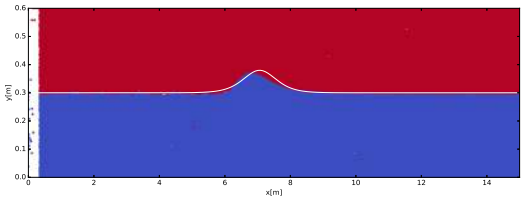

(a) Propagation of soliton at $t = 5$ s.

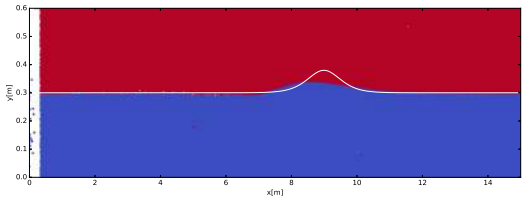

(b) Propagation of soliton at $t = 6$ s.

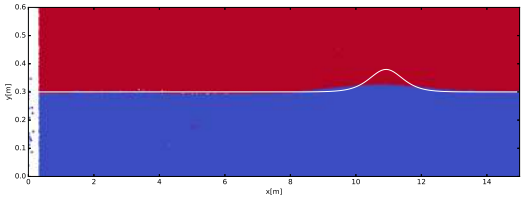

(c) Propagation of soliton at $t = 7$ s.

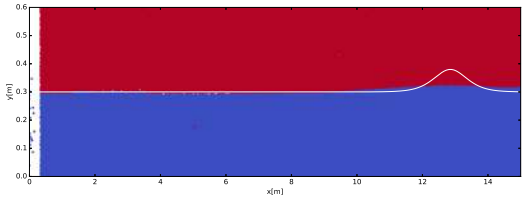

(d) Propagation of soliton at $t = 8$ s.

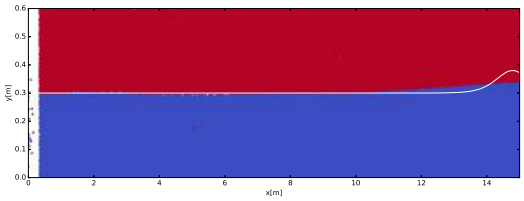

(e) Propagation of soliton at $t = 9$ s.

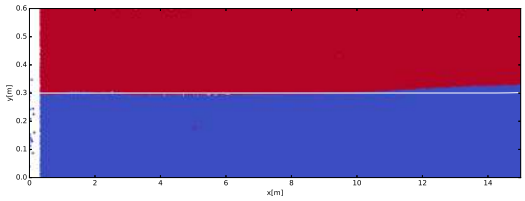

(f) Propagation of soliton at $t = 10$ s.

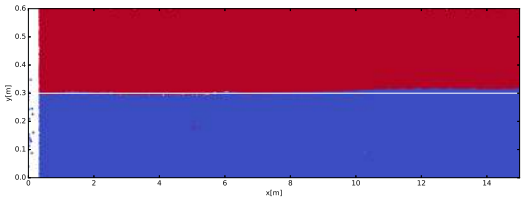

(g) Propagation of soliton at $t = 11$ s.

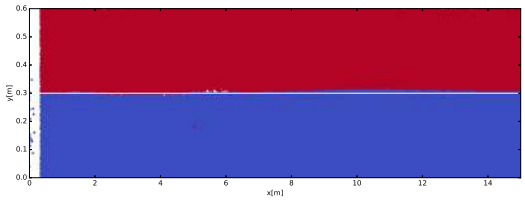

(h) Propagation of soliton at $t = 12$ s.

Figure 5.1: Absorption of soliton $\left(\frac{H}{d} = 0.2667\right)$ in which the same absorption scheme as the case of $\frac{H}{d} = 0.2$ was applied. The wave are apparently absorbed at $t = 12$ s but it leads to the rise of surface elevation at the right side of the tank.

Bibliography

Aknin, D. and Spinneken, J. (2017). A laboratory investigation concerning the superharmonic free wave suppression in shallow and intermediate water conditions. *Coastal Engineering*, 120:112–132.

Andersen, T. L., Clavero, M., Frigaard, P., Losada, M., and Puyol, J. (2016). A new active absorption system and its performance to linear and non-linear waves. *Coastal Engineering*, 114:47–60.

Cao, Y., Beck, R. F., and Schultz, W. W. (1993). An absorbing beach for numerical simulations of nonlinear waves in a wave tank. In *Proc. 8th Intl. Workshop Water Waves and Floating Bodies*, pages 17–20.

Celebl, M., Kim, M., and Beck, R. (1998). Fully nonlinear 3-d numerical wave tank simulation. *Journal of Ship Research*, 42(1):33–45.

Chan, R. (1975). Two dimensional time-dependent calculations of large-amplitude surface gravity waves due to a surface disturbance. In *The First International Conference on Numerical Ship Hydrodynamics*.

Chen, Q., Kelly, D. M., Dimakopoulos, A. S., and Zang, J. (2016). Validation of the picin solver for 2d coastal flows. *Coastal Engineering*, 112:87–98.

Chen, Y., Lee, J., and Eskandarian, A. (2006). *Meshless methods in solid mechanics*. Springer Science & Business Media.

Cherfils, J., Pinon, G., and Rivoalen, E. (2012). Josephine: A parallel sph code for free-surface flows. *Computer Physics Communications*, 183(7):1468–1480.

Cho, Y.-S. (2003). A note on estimation of the jacobian elliptic parameter in cnoidal wave theory. *Ocean engineering*, 30(15):1915–1922.

Dean, R. G. and Dalrymple, R. A. (1991). *Water wave mechanics for engineers and scientists*, volume 2. World Scientific Publishing Co Inc.

Galvin, C. J. (1964). Wave-height prediction for wave generators in shallow water. Technical report, DTIC Document.

Goring, D. G. (1978). *Tsunamis–the propagation of long waves onto a shelf*. PhD thesis, California Institute of Technology.

Hald, T., Frigaard, P., et al. (1997). Performance of active wave absorption systems: comparison of wave gauge and velocity meter based systems. In *The Seventh International Offshore and Polar Engineering Conference*. International Society of Offshore and Polar Engineers.

Harlow, F. H. (1962). The particle-in-cell method for numerical solution of problems in fluid dynamics. Technical report, Los Alamos Scientific Lab., N. Mex.

Havelock, T. (1929). Lix. forced surface-waves on water. *The London, Edinburgh, and Dublin Philosophical Magazine and Journal of Science*, 8(51):569–576.

Herbich, J. B. (1956). Experimental studies of wave filters and absorbers.

Higuera, P., Lara, J. L., and Losada, I. J. (2013). Realistic wave generation and active wave absorption for navier–stokes models: Application to openfoam®. *Coastal Engineering*, 71:102–118.

Idelsohn, S. R., Oñate, E., and Pin, F. D. (2004). The particle finite element method: a powerful tool to solve incompressible flows with free-surfaces and breaking waves. *International journal for numerical methods in engineering*, 61(7):964–989.

Ingram, D. M., Causon, D. M., and Mingham, C. G. (2003). Developments in cartesian cut cell methods. *Mathematics and Computers in Simulation*, 61(3):561–572.

Israeli, M. and Orszag, S. A. (1981). Approximation of radiation boundary conditions. *Journal of computational physics*, 41(1):115–135.

Jacobsen, N. G., Fuhrman, D. R., and Fredsøe, J. (2012). A wave generation toolbox for the open-source cfd library: Openfoam®. *International Journal for Numerical Methods in Fluids*, 70(9):1073–1088.

Katell, G. and Eric, B. (2002). Accuracy of solitary wave generation by a piston wave maker. *journal of hydraulic research*, 40(3):321–331.

Kelly, D. M., Chen, Q., and Zang, J. (2015). Picin: a particle-in-cell solver for incompressible free surface flows with two-way fluid-solid coupling. *SIAM Journal on Scientific Computing*, 37(3):B403–B424.

Kim, M. W., Koo, W., and Hong, S. Y. (2014). Numerical analysis of various artificial damping schemes in a three-dimensional numerical wave tank. *Ocean Engineering*, 75:165–173.

Labeur, R. J. and Wells, G. N. (2012). Energy stable and momentum conserving hybrid finite element method for the incompressible navier–stokes equations. *SIAM Journal on Scientific Computing*, 34(2):A889–A913.

Larsen, J. and Dancy, H. (1983). Open boundaries in short wave simulations—a new approach. *Coastal Engineering*, 7(3):285–297.

Lin, P. and Liu, P. L.-F. (1999). Internal wave-maker for navier-stokes equations models. *Journal of waterway, port, coastal, and ocean engineering*, 125(4):207–215.

Liu, G.-R. and Liu, M. B. (2003). *Smoothed particle hydrodynamics: a meshfree particle method*. World Scientific.

Madsen, O. S. (1971). On the generation of long waves. *Journal of Geophysical Research*, 76(36):8672–8683.

Malek-Mohammadi, S. and Testik, F. Y. (2010). New methodology for laboratory generation of solitary waves. *Journal of Waterway, Port, Coastal, and Ocean Engineering*, 136(5):286–294.

Maljaars, J. (2016). *A hybrid particle-mesh method for simulating free surface flows*.

Mast, C. M. (2013). *Modeling landslide-induced flow interactions with structures using the material point method*. PhD thesis, University of Washington.

Mei, C. C., Stiassnie, M., and Yue, D. K.-P. (1989). *Theory and Applications of Ocean Surface Waves: Part 1: Linear Aspects Part 2: Nonlinear Aspects*. World Scientific.

Milgram, J. H. (1965). Compliant water wave absorbers. Technical report, DTIC Document.

Milgram, J. H. (1970). Active water-wave absorbers. *Journal of Fluid Mechanics*, 42(04):845–859.

Multer, R. and Galvin, C. (1967). Secondary waves: periodic waves of nonpermanent form. *EOS*, 48:209–29.

Oliveira, T. C., Sánchez-Arcilla, A., and Gironella, X. (2012). Simulation of wave overtopping of maritime structures in a numerical wave flume. *Journal of Applied Mathematics*, 2012.

Petit, H., Klopman, G., and Otta, A. (1993). Laboratory wave generation: A second-order theory for regular and irregular waves in wave channels. Technical report, Deltares (WL).

Pilch, M. (1953). *Laboratory Wave-generating Apparatus: Translation of a Series of French Articles from La Houille Blanche*. St. Anthony Falls Hydraulic Lab., University of Minnesota.

Russell, A. J. S. (1844). Report on waves, report of the 14th meeting of the british association for the advancement of science, 311-390.

Salter, S. H. (1981). Absorbing wave-makers and wide tanks. In *Directional Wave Spectra Applications:*, pages 185–202. ASCE.

Schäffer, H. A. (1996). Second-order wavemaker theory for irregular waves. *Ocean Engineering*, 23(1):47–88.

Shibata, K., Koshizuka, S., Sakai, M., and Tanizawa, K. (2011). Transparent boundary condition for simulating nonlinear water waves by a particle method. *Ocean Engineering*, 38(16):1839–1848.

Spinneken, J., Christou, M., and Swan, C. (2014). Force-controlled absorption in a fully-nonlinear numerical wave tank. *Journal of Computational Physics*, 272:127–148.

Spinneken, J., Swan, C., et al. (2009). Wave generation and absorption using force-controlled wave machines. In *The Nineteenth International Offshore and Polar Engineering Conference*. International Society of Offshore and Polar Engineers.

Troch, P. and De Rouck, J. (1999a). An active wave generating–absorbing boundary condition for vof type numerical model. *Coastal Engineering*, 38(4):223–247.

Troch, P. and De Rouck, J. (1999b). A numerical wave flume for wave interaction with rubble mound breakwaters. *Bulletin of the Permanent International Association of Navigation Congresses*, (101):15–21.

Ursell, F., Dean, R. G., and Yu, Y. (1960). Forced small-amplitude water waves: a comparison of theory and experiment. *Journal of Fluid Mechanics*, 7(01):33–52.

Wazwaz, A.-M. (2010). *Partial differential equations and solitary waves theory*. Springer Science & Business Media.

Wu, N.-J., Tsay, T.-K., and Chen, Y.-Y. (2014). Generation of stable solitary waves by a piston-type wave maker. *Wave Motion*, 51(2):240–255.

Zhang, H. and Schäffer, H. A. (2007). Approximate stream function wavemaker theory for highly non-linear waves in wave flumes. *Ocean engineering*, 34(8):1290–1302.